Journal of Applied Physics

RESEARCH ARTICLE | FEBRUARY 23 2024

Multi-scale modeling of shock initiation of a pressed energetic material III: Effect of Arrhenius chemical kinetic rates on macro-scale shock sensitivity

P. Parepalli ; Yen T. Nguyen ; O. Sen ; D. B. Hardin ; C. D. Molek ; E. J. Welle ; H. S. Udaykumar

J. Appl. Phys. 135, 085106 (2024)
https://doi.org/10.1063/5.0187735

AIP Publishing

Journal of Applied Physics ARTICLE pubs.aip.org/aip/jap

Multi-scale modeling of shock initiation of a pressed energetic material III: Effect of Arrhenius chemical kinetic rates on macro-scale shock sensitivity

Cite as: J. Appl. Phys. **135**, 085106 (2024); doi: 10.1063/5.0187735
Submitted: 15 November 2023 · Accepted: 1 February 2024 ·
Published Online: 23 February 2024

P. Parepalli,[1] Yen T. Nguyen,[1] O. Sen,[1] D. B. Hardin,[2] C. D. Molek,[2] E. J. Welle,[2] and H. S. Udaykumar[1,a)]

AFFILIATIONS

[1]Department of Mechanical and Industrial Engineering, The University of Iowa, Iowa City, Iowa 52242, USA
[2]Air Force Research Laboratory, Eglin AFB, Eglin, Florida 32542, USA

[a)]**Author to whom correspondence should be addressed:** hs-kumar@uiowa.edu

ABSTRACT

Multi-scale predictive models for the shock sensitivity of energetic materials connect energy localization ("hotspots") in the microstructure to macro-scale detonation phenomena. Calculations of hotspot ignition and growth rely on models for chemical reaction rates expressed in Arrhenius forms; these chemical kinetic models, therefore, are foundational to the construction of physics-based, simulation-derived meso-informed closure (reactive burn) models. However, even for commonly used energetic materials (e.g., HMX in this paper) there are a wide variety of reaction rate models available. These available reaction rate models produce reaction time scales that vary by several orders of magnitude. From a multi-scale modeling standpoint, it is important to determine which model best represents the reactive response of the material. In this paper, we examine three global Arrhenius-form rate models that span the range of reaction time scales, namely, the Tarver 3-equation, the Henson 1-equation, and the Menikoff 1-equation models. They are employed in a meso-informed ignition and growth model which allows for connecting meso-scale hotspot dynamics to macro-scale shock-to-detonation transition. The ability of the three reaction models to reproduce experimentally observed sensitivity is assessed by comparing the predicted criticality envelope (Walker–Wasley curve) with experimental data for pressed HMX Class V microstructures. The results provide a guideline for model developers on the plausible range of time-to-ignition that are produced by physically correct Arrhenius rate models for HMX.

I. INTRODUCTION

The sensitivity of heterogeneous energetic (HE) materials is a function of both their chemical (molecular) and physical (micro-) structure.[1] The chemistry of a wide range of energetic materials is underpinned by the molecular structures of the CHNO compounds such as TATB (1,3,5-triamino-2,4,6-trinitrobenzene), RDX (1,3,5-trinitro-1,3,5-triazine), HMX (1,3,5,7-tetranitro-1,3,5,7-tetrazocine), PETN (pentaerythritol tetranitrate), etc.[2]. Under suitable loading conditions, these molecules decompose to release energy on different time scales, ranging from the slowest release in the case of TATB to rapid release in PETN, with reactivity of the other molecules book-ended by these extremes.[2] In addition to molecular structures, the physical composition (crystal/binder fraction, additives, etc.) and microstructural features (grain sizes, defect distribution, etc.) in a formulation of HE materials plays a key role in determining their sensitivity to external loads. Reactions are triggered at defects in the microstructure and advance into the unreacted sample, leading to deflagration-to-detonation (DDT[3,4]) or shock-to-detonation (SDT[1,5,6]) scenarios; prediction of these events is crucial from a safety and performance standpoint. Such predictive capabilities call for connecting molecular scale and meso-scale (microstructural level) processes to express the effect of "sub-grid"

physics and chemistry at the observable/system/macro-scale. In this work, we perform such a multi-scale analysis, investigating the interplay of reaction chemistry (molecular scale processes) and microstructural heterogeneities (meso-scale processes) in determining the experimentally observed shock response of one specific type of HE materials, namely, neat-pressed HMX.[7,8]

Macro-scale sensitivity of HE materials is strongly dependent on energy localization in the microstructure.[9–11] Meso-scale phenomena such as pore collapse, friction between crystals, and formation of shear bands, lead to localized temperature excursions or hotspots.[12,13] Several aspects of structure–property–performance linkages[1,14] for HE materials have begun to be clarified in the past two decades, following seminal work highlighting the importance of defects in localizing energy.[15–17] Broadly, resolved meso-scale simulations and experiments have provided the following insights into microstructural influences on initiation sensitivity:

(1) Porosity enhances the sensitivity of HE materials as shown in experiments on a variety of HE formulations.[18,19]
(2) Pores or voids in a HE material can be found within the energetic crystals, in the extra-crystalline regions in pressed materials, and in the binder phase in PBXs (plastic bonded explosives).[20–24] Void collapse in the intra- and extra-crystalline regions can initiate reactions in the energetic component (crystal phase) in pressed as well as PBX materials.[25,26]
(3) Voids at crystal–binder interfaces, perhaps due to debonding of the binder from the crystal, can also collapse under suitable loading conditions, initiating hotspots. Such hotspots are potentially weaker than those presented at intra- or inter-crystalline void collapse sites.[20]
(4) Void sizes determine whether hotspots formed by their collapse become critical,[12] i.e., producing a sustained deflagration front. For voids smaller than a certain size, collapse leads to rather weak hotspots that are quenched by thermal diffusion, whereas voids larger than a critical size range may not collapse under a given shock load. Thus, there is a range of voids sizes that is most effective in generating critical hotspots.[27] In most cases, the range of sensitive void sizes is of the order of a micron in diameter.[15]
(5) Void shapes play a significant role in energy localization, with elongated voids leading to large, intense hotspots[28–31]; however, the orientation of elongated voids is highly significant.[28,29] Elongated voids oriented nearly parallel to the direction of shock propagation produce the most intense hotspots, whereas voids oriented normal to the shock propagation direction produce weaker hotspots. Part I of the current series described the physics underlying the complex-shaped void collapse and hotspot formation.[28] Voids that are commonly found in microstructures have highly contorted (so-called wormhole type[32]) shapes; the orientation of the branches of the voids with respect to the shock determines the shape and size of the resulting hotspot.[28,33] Void branches that are oriented unfavorably can remain dormant while favorably oriented branches can ignite.
(6) Void–void interactions are important when the porosity consists of large voids (in the range of 10 μm in size) but less important for smaller void sizes (of the range of μm or below), Part II of the current series described the physics underlying the void–void interaction effects.[34]
(7) Shear bands can arise in HE materials even in the absence of porosity and can form sites for hotspot initiation;[11] however, the resulting hotspots are likely weaker than void collapse generated ones.[35] In combination with voids however, shear bands can significantly enhance the volume of heated materials, enhancing the rate of heat release.

All of the above effects of the microstructure of a HE formulation couple in complex ways with reaction chemistry. Hotspot ignition and growth is sensitive to the temperature which appears in the chemical kinetics model (typically of the Arrhenius form) for decomposition of the HE. Variations in the reaction models can lead to variations in sensitivity predictions,[36] but despite the surmised strong dependency, to date the effects of reaction models on the macro-scale sensitivity of HEs have not been analyzed fully. This is because, in practice, the sensitivity of an energetic material such as HMX is determined in macro-scale experiments. Prediction of sensitivity at the macro-scale is the "proof of the pudding" as it were, to indicate which reaction rate model should be employed, i.e., establishing which reaction model is "correct" is dictated by a "top-down" analysis guided by macro-scale experiments. This work undertakes the task of performing this top-down analysis, i.e., we start with the experimentally observed macro-scale initiation threshold results for a pressed HMX material[8] and examine which reaction models produce the best agreement with the experimental sensitivity curves. In other words, here the ground truth for the assessment is taken to be the ability of the models to best match the James/Walker–Wasley/go-no-go envelope[37,38] for a pressed HMX material. Required reaction model complexity and linkages to Henson's 1-step global kinetics model were previously investigated by our team.[39] There, we concluded that Ln(Z) values exist that exhibit the measured experimental trends and warranted further study. Additionally, the model results suggested that Ln(Z) values were in reasonable agreement with those presented previously by Henson *et al.*[40] Figure 1 illustrates the multiscale modeling approach used in the current work, and the route by which the variability in the reaction models influence meso- and macro-scale quantities of interest (QoIs) for a given pressed HMX sample.

The chemical decomposition of HMX has been studied by several researchers and a variety of models have been proposed.[36] Handley *et al.*[1] review these models for HMX, for which (among CHNO molecules) the most attention has been paid to developing and evaluating reaction rate models. Based on a review of several models, Handley *et al.* state that the most popular Arrhenius form models, namely, Henson's 1-step[40] global model and Tarver's 3-step[2,41] model fall short of reproducing key experimental time to explosion data and fail to produce steady 1D propagating detonation waves. Menikoff's[42] modifications of the reaction rate were intended to produce 1D sustained detonations. However, over a range of temperatures, the Tarver and Menikoff models differ from the Henson global curve-fit by several orders of magnitude in their reaction time predictions. In fact, Henson's[40] fit to a wide range of experiments, to obtain a global one-equation kinetic model, remains a reliable guide for the chemical decomposition of HMX. The situation regarding the reaction models is even less well understood when they are employed to calculate the ignition and growth of hotspots produced due to shock-induced void collapse. Rai

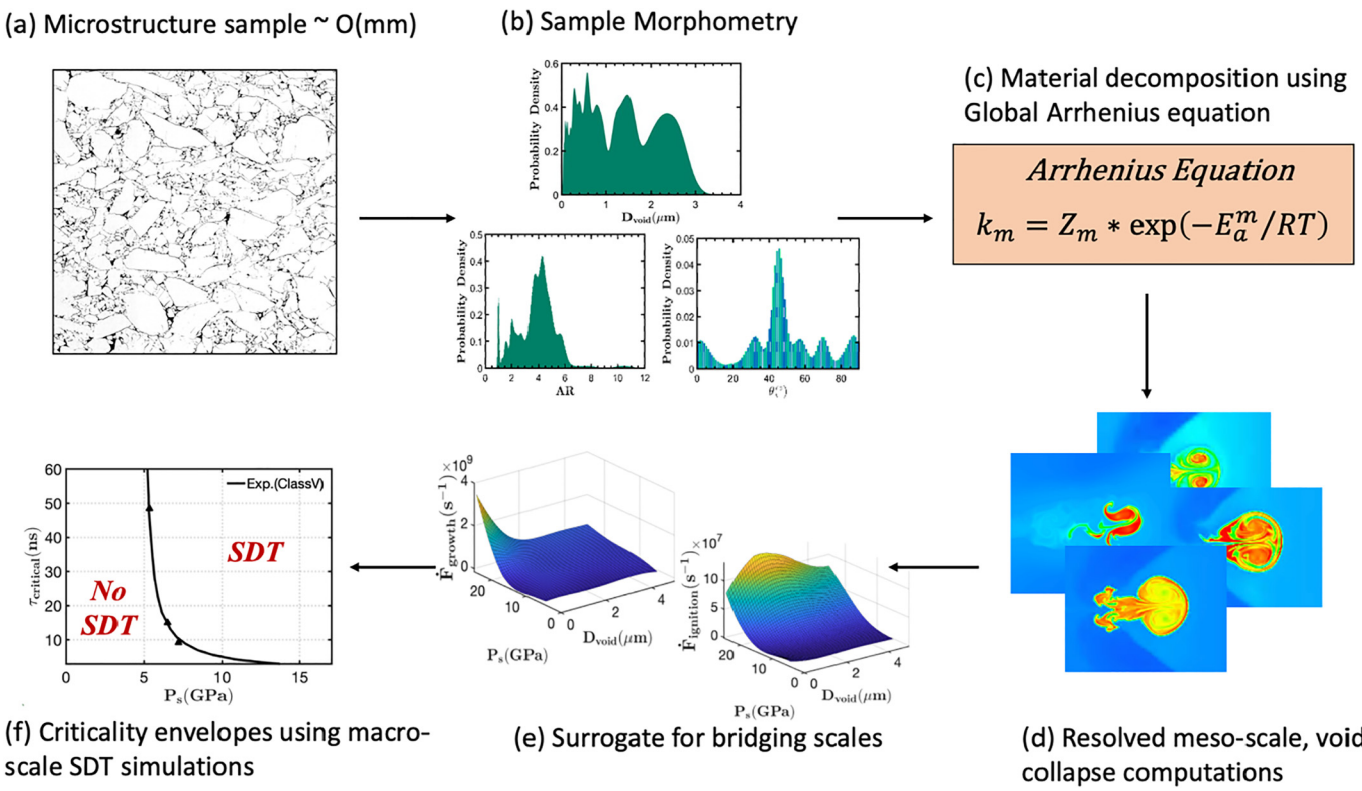

FIG. 1. Schematic representation of the multiscale modeling workflow. The framework involves performing high-fidelity resolved mesoscale simulations of reactive void-collapse calculations. The model uses: (a) an imaged pressed HMX microstructure, and (b) extracts the morphometric data. (c) The decomposition of the HE material (HMX in the current work) from solid energetic crystals to gaseous products is modeled using the global Arrhenius form of the chemical reaction model. (d) The numerical experiments are reactive meso-scale computations of collapse of voids. (e) The ensemble of mesoscale computations is then used to train a surrogate model to quantify the reaction progress variable ($\dot{F}$) in the macro-scale model using the modified Bayesian Kriging method. (f) The macro-scale computational model probes the surrogate on the fly and transitions the material from a shock to a detonation Hugoniot for predictive modeling of SDT.

et al.[36] studied five different chemical decomposition models to understand the effects of chemical properties of HMX on hotspot formation. These reaction models include the above named three commonly used models as well as more sophisticated multi-step models. They showed that of the five models, the Tarver-3 step (T3) and Henson 1-step (H1) models are in fairly good agreement with regard to ignition and growth of hotspots; for these two models critical hotspots were achieved for lower values of shock pressure. Whereas, the Menikoff 1-step (M1) model behaved quite differently from the T3 and H1 models; the criticality conditions for hotspot ignition and growth were achieved at much higher pressures than for the other models. The more sophisticated multi-step models deviated from these three simpler semi-phenomenological global kinetics models and their reactive response lay in between the criticality responses of the H1/T3 and M1 models. These varied responses of the range of reaction chemistry models offer the modeler no basis for judging their suitability for reactive void collapse calculations. Thus, while Rai *et al.*[36] pointed to these differences in the criticality curves and hotspots yielded by the available models, it was not possible for them to indicate which, if any, of these three models should be chosen to represent energy localization and reactive dynamics in meso-scale simulations in a multi-scale predictive workflow, as in Fig. 1.

In the current study, the three simpler, global reaction models in Arrhenius model forms (see Fig. 1), T3, H1, and M1, are used to understand the differences in the hotspot initiation and growth behavior at the meso-scale and to quantify their effects on the sensitivity predictions at the macro-scale. In addition to examining the macro-scale effects of reaction kinetics models, we also seek to understand the interplay of chemistry and microstructures. To this end, this paper performs macro-scale sensitivity predictions for two different types of HMX materials,[8,37] class V and R10. These two classes of HMX materials differ in the initial particle sizes and their distributions (see Fig. 2) utilized in forming the pressed samples, therefore presenting different porosities and void size distributions. We perform a full multi-scale analysis, as shown in Fig. 1, of the performance of these two classes of energetic materials, utilizing the microstructural images and corresponding experimental James envelope developed by Welle *et al.*[8,37]. The availability of the macro-scale sensitivity data as well as microstructural details

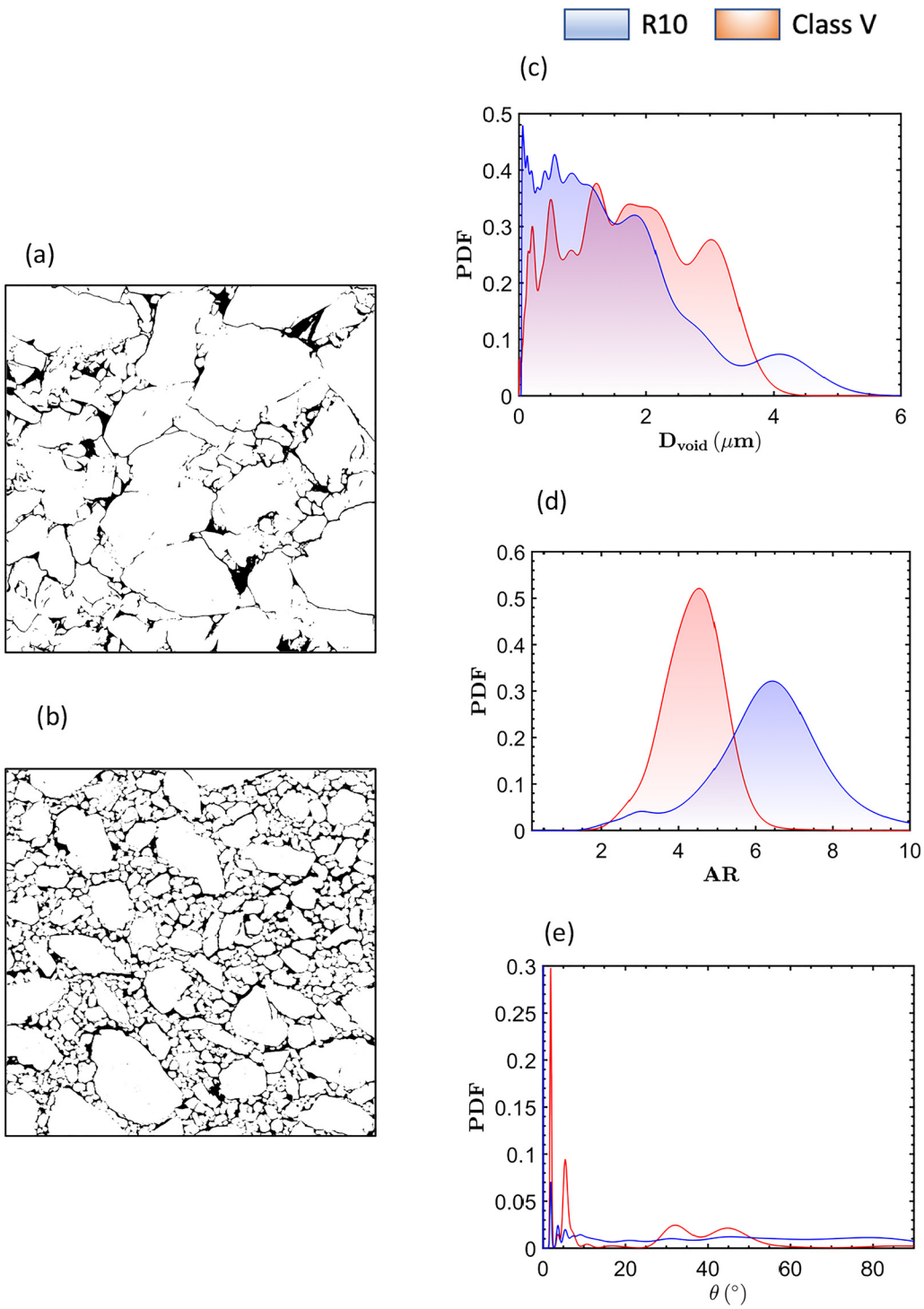

FIG. 2. Microstructures and morphometry of pressed HMX. Representative samples shown for (a) pressed R10 HMX material ($25.0 \times 25.0\,\mu m^2$) and (b) pressed Class V HMX material ($40.0 \times 40.0\,\mu m^2$). Porosity weighted probability density distributions (pdfs) of sample morphometry for (c) void diameter, D_{void} (d) aspect ratio, AR and (e) void orientation, θ.

enables study of the interplay between chemistry and meso-scale dynamics for class V HMX. We examine the combined effects of reaction chemistry models and the rather subtle differences in the microstructure between two classes of porous HE materials, i.e., class V and R10.

The structure of the paper is as follows. We first briefly outline the framework of the meso-informed ignition and growth model (MES-IG),[43] which connects the meso-scale reactive dynamics with the macro-scale computational model. Section II (Methods) presents a brief account of the models and methods employed in the calculations. Section III (Results) shows the comparison between the three reaction models T3, H1, and M1 for criticality conditions required for hotspot initiation in reactive void collapse calculations. Ensembles of reactive void collapse calculations are then performed to construct surrogate models using the three reaction models. Lastly the macro-scale sensitivity predictions are performed using the three surrogate models for two material microstructures and compared with the experimental data. Section IV (Conclusions) summarizes the effects of porosity on macro-scale sensitivity and the interplay between reaction kinetic models and microstructures.

II. METHODS

Multi-scale modeling involves solution of the following governing equations for thermo-mechanics of a reactive condensed phase material.

A. Governing equations

The conservation laws for mass, momentum, energy, and species in the Eulerian setting[44,45] are

$$\frac{\partial \rho}{\partial t} + \frac{\partial (\rho u_i)}{\partial x_i} = 0, \tag{1}$$

$$\frac{\partial (\rho u_i)}{\partial t} + \frac{\partial (\rho u_i u_j - \sigma_{ij})}{\partial x_j} = 0, \tag{2}$$

$$\frac{\partial (\rho E)}{\partial t} + \frac{\partial (\rho E u_j - \sigma_{ij} u_i)}{\partial x_j} = \chi_S \dot{\mathcal{E}}, \tag{3}$$

$$\frac{\partial (\rho S_{ij})}{\partial t} + \frac{\partial (\rho S_{ij} u_k)}{\partial x_k} + \frac{2}{3}\rho G D_{kk}\delta_{ij} - 2\rho G D_{ij} = 0, \tag{4}$$

where ρ and u_i, respectively, denote the density and the velocity components, $E = e + \frac{1}{2}u_i u_i$ is the specific total energy, e is the specific internal energy, and σ_{ij} is the Cauchy stress of the form, $\sigma_{ij} = S_{ij} - p\delta_{ij}$ where S_{ij} is the deviatoric stress tensor, p is the pressure, δ_{ij} is the Kronecker delta, and D_{ij} denotes the strain-rate tensor. The source term $\dot{\mathcal{E}}$ contains the heat generated by chemical reaction, with the parameter χ_S controlling the model at the two different scales (meso-/macro-) at which the calculations are performed, as will be described below.

1. Constitutive models for HMX

The material models for HMX used to perform reactive void collapse simulations are based on values provided by Menikoff and Sewell.[46,47] The pressure (p) is obtained using a Mie–Grüneisen equation of state,

$$p = p_c + \frac{\Gamma(V)}{V}(e - e_c(V)), \tag{5}$$

with a Birch–Murnaghan form for the cold or athermal pressure p_c as a function of specific volume $\mathrm{V}\left(=\frac{1}{\rho}\right)$,

$$p_c(V) = \frac{3}{2}K_0\left(\left(\frac{V}{V_0}\right)^{-\frac{7}{3}} - \left(\frac{V}{V_0}\right)^{-\frac{5}{3}}\right) \times \left(1 + \frac{3}{4}(K'_0 - 4)\left(\left(\frac{V}{V_0}\right)^{-\frac{2}{3}} - 1\right)\right). \tag{6}$$

The athermal contribution to the specific internal energy e_c is then

$$e_c(V) = e_0 - \int_{V_0}^{V} p_c(V)dV. \tag{7}$$

The Grüneisen coefficient is

$$\Gamma(V) = -\frac{V}{\theta}\frac{d\theta}{dV} = a + b\frac{V}{V_0}. \tag{8}$$

$\theta(V)$ is the Debye temperature given by the expression

$$\theta(V) = \theta_0\left(\frac{V_0}{V}\right)^{\Gamma}\exp\left(\frac{b(V_0 - V)}{V}\right). \tag{9}$$

The reference condition (subscript 0) is the ambient at 298 K. The equations of state properties were obtained from Menikoff and Sewell.[46]

HMX is modeled as an elastic perfectly-plastic material; the values for the shear modulus and yield stress are obtained from Ref. 46 and listed in Table I. Void collapse under shock loading can lead to the melting of HMX; therefore thermal softening of HMX is modeled using the Kraut–Kennedy relation for HMX,

$$T_m = T_{m,0}\left(1 + a_1\frac{\Delta V}{V_0}\right). \tag{10}$$

The material constants and fitting constants a, b, and a_1 in the equations above are listed in Table I. Once the temperature exceeds the melting point of HMX, the deviatoric strength terms are set to zero, i.e., G = 0 when $T \geq T_m$.

2. Chemical decomposition models for HMX

The three reaction models evaluated are as follows:

1. **H1:** The Henson 1-step reaction model is based on fitting a global Arrhenius form to the time of reaction across a wide

TABLE I. Constitutive properties of HMX.

Property	Value
ρ_{ref}(kg/m^3)	1900
G(GPa)	12
K_{T0}(GPa)	16.5
K'_{T0}(GPa)	8.7
β(K^{-1})	1.31×10^{-4}
σ_Y(GPa)	0.26
T_{m0}(K)	551
α	1.533
A	1.1
B	−0.2
a1	1.533

TABLE II. Chemical reaction rate parameters for the three HMX chemical decomposition models.

Reaction No.	Frequency factor, lnZ (s^{-1})	Activation energy E_a (kcal/mol)	Energy release Q(kcal/mol) at 298 K
Henson—1 Step (H1) Model			
1	29.35	35.61	−414.62
Menikoff—1 Step (M1) Model			
1	26.36	35.57	−353.91
Tarver—3 Step (T3) Model			
1	48.7	52.7	29.62
2	37.3	44.1	−88.85
3	28.1	34.1	−355.39

array of experiments collated and analyzed by Henson *et al.*[40]. In this model, solid HMX is decomposed into final gases in a single step,

$$HMX(\text{solid})(C_4H_8N_8O_8) \rightarrow \text{final gases}(N_2, CO, CO_2, H_2O). \tag{11}$$

2. **M1:** Menikoff[42] followed the H1 approach to model the decomposition of solid HMX to final gaseous products, as in Eq. (11). However, the pre-factor of the H1 global rate constant was modified to match the adiabatic induction time for the HMX-based energetic material PBX 9501.
3. **T3:** The Tarver model[41] is a semi-phenomenological multistep model. It involves a three-step reaction mechanism where HMX is decomposed into fragments and intermediate gases before leading to final gaseous products. This global model was obtained by fitting to experimental data using a one-dimensional thermal explosion (ODTX) calculation by matching the time to explosion with the experimental data. The temperature range over which the data were fit is 800–1200 K. This temperature range is at the lower end of the void collapse generated hotspot temperature and therefore its use in the current meso-scale simulations implies an extrapolation to higher temperatures. The three-step reactions are as follows:

Reaction 1:

$$HMX(\text{solid})(C_4H_8N_8O_8) \xrightarrow{1} \text{fragments}(CH_2NNO_2) \tag{12}$$

Reaction 2:

$$\text{fragments}(CH_2NNO_2) \xrightarrow{2} \text{initial gases}(CH_2O, N_2O, HCN, HNO_2). \tag{13}$$

Reaction 3:

$$\text{initial gases}(CH_2O, N_2O, HCN, HNO_2) \xrightarrow{3} \text{final gases}(N_2, CO, CO_2, H_2O). \tag{14}$$

In each of the above models, the reaction rate constants for the mth reaction k_m are in the Arrhenius form,

$$k_m = Z_m{}^* \exp(-E_a^m/RT). \tag{15}$$

Table II shows the chemical reaction rate parameters for the three reaction models.

In the present calculations, transport of the reactant and product species follows, for the lth species,

$$\frac{\partial \rho Y_l}{\partial t} + \frac{\partial}{\partial x_j}(\rho u_j Y_l) = \rho \dot{Y}_l. \tag{16}$$

Y_l is the species mass fractions/mole fractions/molar concentrations (depending on the model[36]) of the lth species and $\dot{Y}_l$ is the corresponding production rate source term. The species are designated as follows, $l = 1$ corresponds to solid HMX, $l = 2$ to fragments of HMX (CH_2NNO_2), $l = 3$ to initial gases (CH_2O, N_2O, HCN, HNO_2), and $l = 4$ to final product gases (N_2, CO, CO_2, H_2O).

The species production rates are given by

$$\dot{Y}_l = k_{m-1} Y_{l-1}^{\nu_{l-1,m-1}} - k_m Y_l^{\nu_{l,m}}, \tag{17}$$

where $\nu_{l,m}$ is the stoichiometric coefficient for the lth species in the mth reaction.

The temperature field is calculated in a Strang splitting approach. The predictor update calculates the temperature from the internal energy obtained by solving Eq. (3) for E and using $e = E - \frac{1}{2} u_j u_j$. Then, in the first step, the intermediate temperature is obtained from

$$T^*(V, e) = T_0 \left(\frac{V}{V_0}\right)^{\Gamma} + \left(\frac{e - e_c(V)}{C_v}\right). \tag{18}$$

Here, the first term on the right hand side is due to isentropic compression,[46] and the second term is due to the caloric equation of state. The specific heat C_v is a function of temperature, expressed

TABLE III. Thermal properties for HMX.

Property	HMX	Fragments	Gases1	Gases2
Heat capacity [cal/(g K)] at				
293 K	0.24	0.22	0.24	0.27
433 K	0.34	0.31	0.27	0.28
533 K	0.40	0.36	0.29	0.29
623 K	0.46	0.42	0.31	0.30
773 K	0.55	0.50	0.35	0.31
>1273 K	0.55	0.50	0.42	0.35
Thermal conductivity [cal/(cm s K)] at				
293 K	1.23×10^{-3}	6.50×10^{-3}	1.0×10^{-4}	1.0×10^{-4}
433 K	9.70×10^{-4}	5.00×10^{-4}	1.0×10^{-4}	1.0×10^{-4}
533 K	8.10×10^{-4}	4.00×10^{-4}	1.0×10^{-4}	1.0×10^{-4}
>623 K	7.00×10^{-4}	3.00×10^{-4}	1.0×10^{-4}	1.0×10^{-4}
Heat of formation at 298 K (cal/g)	+61.0	+161.0	−139.0	−1339.0

in the form

$$C_v(\tilde{T}) = \frac{\tilde{T}^3}{C_0 + C_1\tilde{T} + C_2\tilde{T}^2 + C_3\tilde{T}^3}, \tag{19}$$

where $\tilde{T} = \frac{T^*}{\theta(V)}$ is the normalized temperature with respect to the Debye temperature given in Eq. (9).

The local rate of change of temperature in a control volume due to chemical reaction and heat conduction is then calculated in the second step by solving the evolution equation,

$$\rho C_v \frac{T^{n+1} - T^*}{\delta t} = -\rho C_v \nabla \cdot (\vec{u}\, T^*) + \dot{Q}_R + k\nabla^2 T^{n+1}, \tag{20}$$

where k is the thermal conductivity of the reaction mixture and $\dot{Q}_R = \sum_m Q_m \dot{Y}_m$ is the total heat release rate from the chemical reaction. The variation of specific heat with temperature is specified for each species as presented in Table III.[41] At the end of the reactive update of the species mass fractions and temperature, the change in internal energy Δe due to chemical reactions and thermal diffusion is computed as follows:

$$\Delta e = C_v\,(T - T^*). \tag{21}$$

The final specific internal energy e is then obtained as $e = e^* + \Delta e$.

B. Multi-scale modeling of shock-to-detonation transition

SCIMITAR3D, a sharp-interface Eulerian reactive dynamics code,[45,48] is employed to solve the above system of equations. The two-dimensional conservation laws of mass, momentum, and energy, along with the evolution of deviatoric stresses and species transport equations are spatially discretized using a third-order ENO scheme.[49] The time integration is performed using a third-order Runge–Kutta scheme.[50] The governing equations contain material properties and reaction mechanisms that are presented by Rai *et al.*[44] for simulating shock-induced deformation of solid HMX, reproduced in Tables I–III. The following components are essential ingredients of a Meso-informed Ignition and Growth (MES-IG)[43] model for HE materials as illustrated in Fig. 1.

Microstructure quantification: Pressed HMX microstructures contain defects in the form of inter- and intra- crystal voids and cracks [Fig. 1(a)]. To predict the sensitivity of the material microstructure, the statistics of the microstructural features are quantified via probability density functions [Fig. 1(b)] using methods described by Roy *et al.*[51] These microstructures were generated by ion-beam nanotomography techniques for explosives, initially developed by Wixom *et al.*[52] and later expanded by Welle *et al.*[8,37] Figures 2(a) and 2(b) show the microstructure images for the two classes of porous HE materials, i.e., class V and R10. Therefore, their sensitivities under shock loading are expected to be different. The probability density functions (pdfs) for the parameters void size (D_{void}), aspect ratio (AR) and orientation (θ) are quantified for each class of material to represent microstructural stochasticity, Figs. 2(c)–2(e). Both class V and R10 have voids centered around $0.1 < D_{void} < 3.0\,\mu$m, Fig. 2(c). The AR pdf Fig. 2(b) for R10 has a peak at AR = 6.5, with aspect ratios of voids ranging from $2 < \mathrm{AR} < 10$ and the AR for class V has a peak at AR = 5.8, with aspect ratios of voids ranging from $2 < \mathrm{AR} < 7.5$. The pdf for the void orientation θ for both the materials is a multimodal distribution shown in Fig. 2(e).

Meso-scale simulations: At the mesoscale, the energy localization or formation of hotspots occurs at the voids and cracks in the material. The Arrhenius models examined in this work govern the decomposition and energy release at the meso-scale [Fig. 1(c)]. To capture this localization of energy, reactive void collapse calculations are performed by explicitly resolving the voids [Fig. 1(d)], with calculations carried through hotspot evolution from the ignition to the mature growth phase.[53]

Surrogate models to bridge meso- and macro-scales: Ensembles of high-resolution reactive void collapse calculations [Fig. 1(d)] are performed to obtain input datasets for surrogate models[29,53] that bridge the energy localization due to the hotspot formation at the

mesoscale to the macroscale response to shock loading. The meso-scale energy localization rate is then encapsulated in surrogate models [Fig. 1(e)] in the form of ignition and growth rate functions $\dot{F}_{ignition/growth} = fcn(\text{shock strength, microstructural paramaters})$.

Macro-scale simulations: At the macroscale, the microstructural heterogeneities (voids, cracks) present in the material are considered to be at the "sub-grid" or unresolved scale. The macro-scale representation of the material is a homogenized mixture of reactants and products. The simulations are performed on a 1D coupon of solid HMX to obtain the critical shock pulse width (correlated with a flyer thickness in experiments[8]) $\tau_{critical}$ as a function of the shock pressure P_s (which is correlated with the flyer momentum). The criticality envelope is plotted as a Walker–Wasley[54] curve in the $P_s - \tau_{critical}$ space [Fig. 1(e)].

Methods for the above components are outlined below, while a detailed description of the methodology can be found in previous works.[14,43] QoIs extracted at the meso- and macro-scales are also described in the following.

C. Meso-scale simulations and extraction of QoIs

A levelset-based sharp interface treatment using a modified ghost fluid approach is used to perform void collapse simulations.[55] Simulations are performed in the configuration shown in Fig. 3(a). Sustained shock loading is imposed at the left end of the domain by specifying the pressure P_s; a void of diameter D_{void} is placed as shown in the figure and collapses as the shock traverses across it. Calculations are carried through to times well beyond the instant of collapse, i.e., into the hotspot ignition and growth regime. The energy localization QoIs are then calculated as follows.

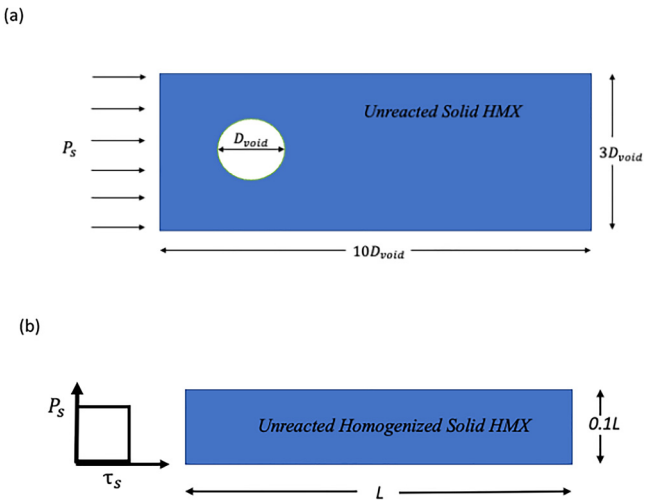

FIG. 3. (a) Setup for performing the highly resolved reactive single circular void collapse computation, containing a void of diameter D_{void}, subjected to a shock of pressure P_s from the west side of the domain boundary. (b) Setup for performing the macroscale computations for SDT. At the macroscale, the unreacted, homogenized, solid HMX material is subjected to a rectangular shock pulse of pressure P_s and shock pulse duration τ_s applied from the west side of the domain boundary.

The chemical decomposition of the HMX material is computed using the three reaction models: H1, M1, and T3. The final reaction product mass fraction is quantified at various stages of void collapse. As in Springer *et al.*,[25] the mass fraction of final reaction products (M_{reacted}) is normalized by the mass of HMX that would nominally fill the void (M_{void}) to define a meso-scale reaction progress variable,

$$F = \frac{M_{reacted}}{M_{void}} = \frac{\int_A \rho Y_4 dA}{\rho_{HMX} A_{void}}, \tag{22}$$

where ρ is the local density, Y_4 is the mass fraction of final gaseous species, ρ_{HMX} is the density of solid HMX, and A_{void} is the area of the void.

The QoIs at the mesoscale are the rates of change of the above reaction product fraction F, calculated at two stages, hotspot ignition ($\dot{F}_{ignition}$) and growth ($\dot{F}_{growth}$). Ensembles of high-resolution reactive void collapse simulations are performed to construct surrogate models[53] for $\dot{F}_{ignition}$ and $\dot{F}_{growth}$. These mesoscale product formation rates are functions of various physical quantities such as the loading P_s, and microstructural features, namely, void size (D_{void}), void aspect ratio (AR), void orientation relative to the nominal imposed shock (θ), and the porosity of the pressed HMX sample (ϕ), i.e.,

$$\dot{F}_{ignition} = f(P_s, D_{void}, AR, \theta, \phi), \tag{23a}$$

$$\dot{F}_{growth} = f(P_s, D_{void}, AR, \theta, \phi). \tag{23b}$$

It is computationally prohibitive to train a surrogate model using meso-scale simulations performed in the five-dimensional parameter space indicated in Eq. (23). To reduce the complexity of the above model, Eq. (23) is decomposed into the following multiplicative form:[43]

$$\dot{F}_{ignition} = \dot{F}^{scv}_{ignition}(P_s, D_{void}) * f^{shape}_{ignition}(AR, \theta) * f^{v-v}_{ignition}(\phi), \tag{24a}$$

$$\dot{F}_{growth} = \dot{F}^{scv}_{growth}(P_s, D_{void}) * f^{shape}_{growth}(AR, \theta) * f^{v-v}_{growth}(\phi). \tag{24b}$$

Here, $\dot{F}^{scv}_{ignition}$ and $\dot{F}^{scv}_{growth}$ are the mesoscale rate of reaction progress in hotspots formed due to the collapse of a single circular void (scv) of diameter D_{void}. The functions $f^{shape}_{ignition}(AR, \theta)$ and $f^{shape}_{growth}(AR, \theta)$ account for the aspect ratio and the orientation of non-circular voids in the microstructure and serve as modifiers for $\dot{F}^{scv}_{ignition}$ and $\dot{F}^{scv}_{growth}$, respectively. The functions $f^{v-v}_{ignition}(\phi)$ and $f^{v-v}_{growth}(\phi)$ are modifiers to convey the influence of void–void interactions in a field of voids with porosity ϕ. The procedure for computing $f^{shape}_{ignition}(AR, \theta)$, $f^{shape}_{growth}(AR, \theta)$, $f^{v-v}_{ignition}(\phi)$ and $f^{v-v}_{growth}(\phi)$ is described in detail in previous works.[14,29]

To examine the effect of the reaction models, we focus on calculating the mesoscale reaction rates from the collapse of single circular voids; $\dot{F}^{scv}_{ignition}$ and $\dot{F}^{scv}_{growth}$ are computed following void collapse using the three reaction models H1, M1, and T3. Figures 4(a)–4(d), respectively, show the time evolution of the void area A_{void}, area of

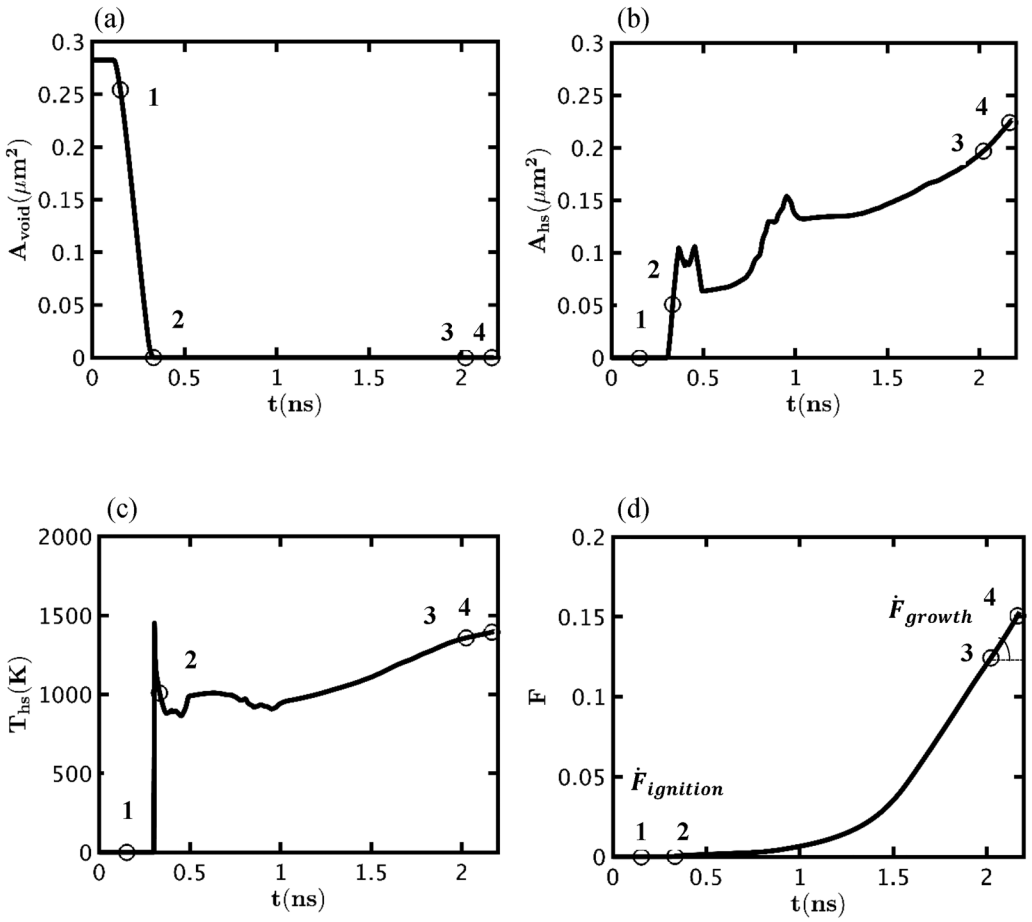

FIG. 4. Procedure for obtaining the quantities of interest $\dot{F}_{ignition}$ and $\dot{F}_{growth}$ for a single circular void collapse of diameter, $D_{void} = 0.6\ \mu$m subjected to a shock pressure, $P_s = 10$ GPa (using T3 model). The figures show the variation of (a) void area, (b) hotspot area, (c) hotspot average temperature, and (d) the product mass fraction F with time. The numbers 1–4 in (a)–(d) indicate different instances of void and hotspot formation/growth. In (d), the time instances for computing the slopes to obtain $\dot{F}_{ignition}$(between points $1-2$) and $\dot{F}_{growth}$(between points 3 and 4) are shown.

hotspot A_{hs}, average temperature of hotspot T_{hs} and product mass fraction F for one instance of void collapse calculation for which $D_{void} = 0.6\ \mu$m and $P_s = 10$ GPa. The temperature contours for the four stages are shown in Fig. 5 (Multimedia available online). The different stages of void collapse are marked in Fig. 4. Stage 1 corresponds to the time when the shock first impinges on the void, initiating its collapse. The area of the void at this stage reduces to 0.9 times the initial area of the void before collapse. Stage 2 corresponds to the time when the void has completely collapsed (taken to be at the time instant when the area of the remaining void is 10% of the initial void area). Stages 1–2 demarcate the ignition phase and $\dot{F}_{ignition}$ is calculated as the average slope of F vs t between these two points. Stage 3 and 4 demarcate the growth phase which corresponds to the time instants when the area of the hotspot reaches a steady growth phase and are taken to be 1.8 and 2 times the area of the initial hotspot formed after complete void collapse. $\dot{F}_{growth}$ is calculated as the average slope of F vs t between points 3 and 4. A detailed description of the procedure for calculating the $\dot{F}_{ignition}$ and $\dot{F}_{growth}$ from hotspot evolution is provided in previous works of Nassar *et al.*[53] and Sen *et al.*[43].

As illustrated in Fig. 1(d), to obtain a surrogate model, ensembles of reactive void collapse computations are performed for various combinations of void diameters in the range of $0.1 < D_{void} < 5\ \mu$m, and shock pressures in the range of $5 < P_s < 25$ GPa. $\dot{F}_{ignition}$ and $\dot{F}_{growth}$ computed from these simulations are used as inputs to train a modified Bayesian Kriging (MBKG) algorithm to assimilate the surrogate model as described bys Sen *et al.*[56]. The surrogates so constructed are supplied to the macroscale computational code to predict SDT in pressed HMX materials at the macro-scale.

D. Macroscale modeling

At the macro-scale, the material is treated as a homogenized mixture of solid HMX and gaseous reaction products. The

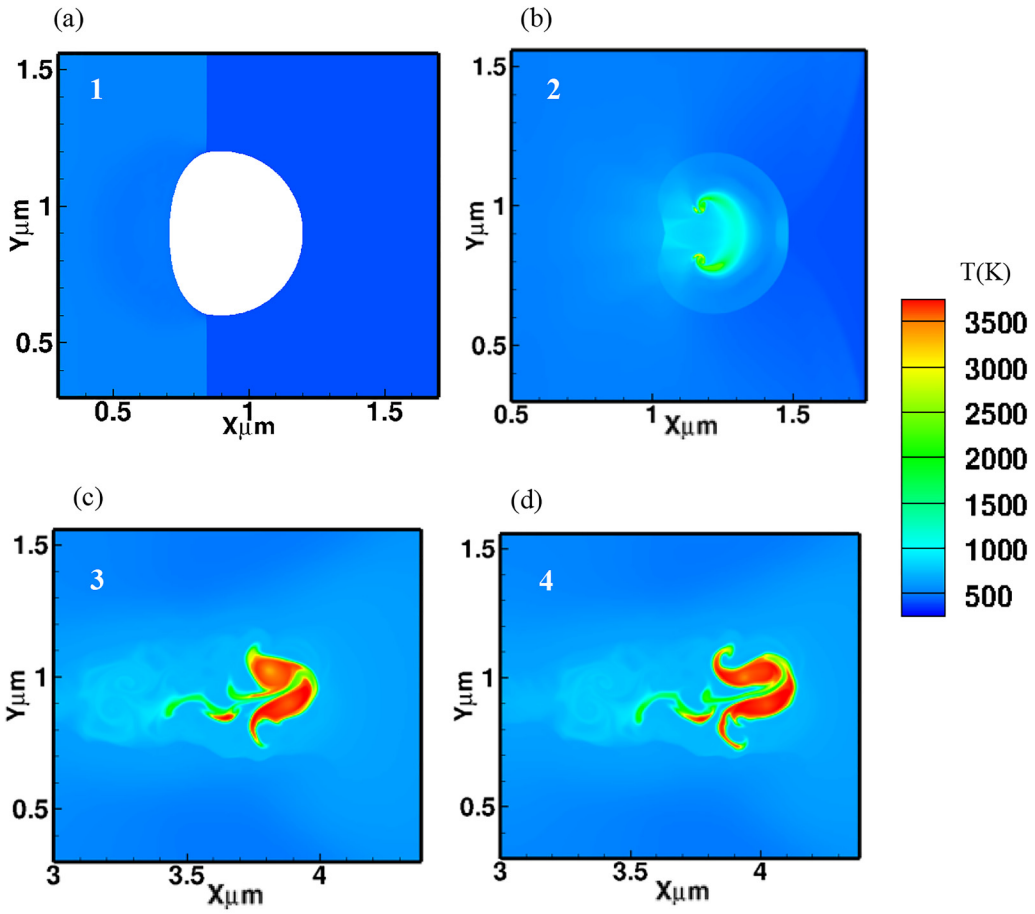

FIG. 5. Temperature contours corresponding to the procedure for obtaining $\dot{F}_{ignition}$ and $\dot{F}_{growth}$ for a single circular void collapse of diameter, $D_{void} = 0.6\ \mu m$ subjected to a shock pressure, $P_s = 10$ GPa (a) instant marked 1 (see Fig. 4), when the void has just started to collapse. ($A_{void} = 90\%$) (b) instant marked 2, when the void has completely collapsed ($A_{void} = 0$) leading to ignition of a hotspot (c) instant marked 3, when the hotspot is the steady growth phase (d) instant marked 4, in the steady growth phase of the hotspot.'(Multimedia view).'

macro-scale computational setup is shown in Fig. 3(b); simulations are performed in a 1D setting corresponding to a flyer impact experiment on a coupon of the pressed energetic material. The state of the mixture is defined by the reaction progress variable λ, which is the mass fraction of the reaction products in a macroscale control volume. When $\lambda = 0$, the material is an unreacted solid explosive; when $\lambda = 1$, the reaction is complete and gaseous products are formed. In the original ignition and growth model,[57] the evolution equation for λ consists of an ignition component, $\lambda_{ignition}$, and a growth component, λ_{growth}. The current MES-IG model follows the form of the original ignition and growth model[57] to close the macroscale system of equations with the reaction progress rate calculated from

$$\frac{d\lambda}{dt} = \dot{\lambda}_{ignition} H(\lambda_{ignition,max} - \lambda) + \dot{\lambda}_{growth} H(\lambda - \lambda_{ignition,max}), \quad (25)$$

where H is the Heaviside function,

$$H(\Delta\lambda) = \begin{matrix} 0 & \text{for } \Delta\lambda < 0, \\ 1 & \text{for } \Delta\lambda \geq 0. \end{matrix} \quad (26)$$

The switching constant, $\lambda_{ignition,max}$ (chosen to be 0.02 in this paper), marks the transition from the ignition to the growth phase. As shown byn Sen *et al.*[43] macroscale variables $\dot{\lambda}_{ignition}$ and $\dot{\lambda}_{growth}$ are obtained from the mesoscale product formation rates $\dot{F}_{ignition}$ and $\dot{F}_{growth}$,

$$\dot{\lambda}_{ignition} = \phi\, \dot{F}_{ignition}, \quad (27a)$$

$$\dot{\lambda}_{growth} = \phi\, \dot{F}_{growth}. \quad (27b)$$

Once the surrogates for $\dot{F}_{ignition}$ and $\dot{F}_{growth}$ are constructed as a function of microstructural metrics, D_{void}, AR, θ, ϕ, to obtain the form shown in Eq. (24), $\dot{\lambda}_{ignition}$ and $\dot{\lambda}_{growth}$ are calculated using Eq. (27) to close the macroscale system of equations.

The rate of transformation of solid HMX to gaseous reaction products in a macro-scale control volume is determined by Eq. (27). At the macroscale, the strength of the material is neglected, i.e., the deviatoric stress S_{ij} in Eq. (4) is not solved for. To calculate the pressure from the equation of state for control volumes where $0 < \lambda < 1$, a mixture treatment is adopted to apply P-T equilibrium between the unreacted and reacted components of the mixture.[43] The equations of state for the solid and the gas phases for obtaining the homogenized pressure p are shown in the Appendix. At the meso-scale, the heat released due to chemical reaction of HMX is modeled via the source term $\dot{\mathcal{E}}$ in Eq. (3) and included in the calculation in the time-split calculation of temperature in Eq. (20). At the macro-scale, $\dot{\mathcal{E}}$ is set to zero and the chemical heat release due to decomposition of HMX into gaseous products is taken into account by transitioning the mixture from a cold, unreacted solid Hugoniot to a product Hugoniot. The calculated value of λ provides the extent of reaction progress in order to affect this transition from unreacted to reacted Hugoniot. The Jones–Wilkins–Lee (JWL) equation of state[58] accounts for the chemical energy release due to detonation. More details on the macroscale modeling can be found in previous work.[43] The procedure for performing the 1D macroscale computations to quantify shock sensitivity is described in the following.

1. Quantifying sensitivity in the Walker-Wasley space through macro-scale simulations

At the macroscale, 1D simulations are performed on a sample of solid HMX materials to calculate the minimum energy needed for SDT in the material. This critical energy threshold required for SDT[37] is identified via a Walker–Wasley envelope in the space parametrized by the shock strength P_s and the shock pulse duration τ_s, defined by

$$E_{cr} = \frac{A_f P_s^2 \tau_s}{Z_f}, \tag{28}$$

where E_{cr} is the critical energy,[38] Z_f and A_f are the impedance and surface area of the flyer, respectively. In practice, τ_s corresponds to the duration of impact a flyer plate (of thickness, w); similarly, P_s is determined by the momentum of the flyer. The macroscale computations are performed for various combinations of shock pulse of pressure P_s and duration τ_s, using the setup shown in Fig. 3(b). In each 1D control volume the local pressure, $p(x, t)$, is tracked over time. The local pressure in a macro-scale control volume (updated by solving the mixture laws shown in the Appendix) is used to compute $\dot{\lambda}_{ignition}$ and $\dot{\lambda}_{growth}$ from the surrogates constructed using data from the meso-scale void collapse generated hotspot simulations. For a given shock strength P_s and pulse duration τ_s, if the local pressure $p(x, t)$ in the control volume, exceeds P_s and reaches the von-Neumann spike pressure, that value of τ_s is labeled as supercritical. On the other hand, if the maximum pressure p in the domain decreases to less than 60% of P_s as the incident shock is attenuated by rarefaction, the corresponding value of τ_s is labeled as a sub-critical pulse duration and the computation is halted. Macroscale computations are repeated for different values of τ_s and the minimum supercritical value of τ_s is taken to be the $\tau_{critical}$ value corresponding to an imposed shock pressure P_s. This procedure leads to the identification of the critical energy [via Eq. (28)] or the go-no-go condition for SDT in the Walker–Wasley space.

2. Monte–Carlo approach for determining $\tau_{critical}$

The method to compute $\tau_{critical}$ for a specific value of shock pressure P_s was described above. Experiments by Welle *et al.*[37,59] show that the critical energy in Eq. (28) varies significantly depending on the microstructure of the material. Therefore, $\tau_{critical}$ is a function of shock pressure P_s and the microstructural parameters D_{void}, AR, θ, ϕ, i.e.,

$$\tau_{critical} = f(P_s, D_{void}, AR, \theta, \phi). \tag{29}$$

In the present work, the microstructure pertains to class V and R10 varieties of pressed HMX materials and is shown in Fig. 2. Using methods described in Roy *et al.*,[51] the statistical measures of the morphological features in the microstructures are quantified in the form of pdfs of the three quantities D_{void}, AR, θ, as shown in Figs. 2(c)–2(e). The macroscale computations are performed for a discrete set of P_s values ranging from 5 to 15 GPa, corresponding to the input pressure ranges in the experiments of Welle *et al.*[8,37]. The values of the morphometric quantities D_{void}, AR and θ for each material are selected such that they lie in the 95% confidence intervals of the respective pdfs, i.e., within the quantile range of $q(0.025) - q(0.975)$. The porosity ϕ is calculated by summing the area occupied by the voids in the domain and normalizing by the area of the sub-sample. From morphometric analysis,[28,51] the porosity for class V was calculated as 14% and for R10 as 7%.

The macro-scale computations are performed for an initial set of random locations in the P_s, D_{void}, AR, θ parameter space. $\tau_{critical}$ for each combination is obtained using the procedure in Sec. II D 1. The Kriging algorithm[60,61] is then used to construct the hypersurface $\tau_{critical} = fcn(P_s, D_{void}, AR \text{ and } \theta)$. To further refine this $\tau_{critical}$ hypersurface, the next set of values of P_s, D_{void}, AR and θ is selected by an adaptive sampling technique in the Kriging algorithm described in Refs. 60 and 61. The $\tau_{critical}$ hypersurface is then sampled at 10^6 Monte–Carlo (MC) points obtained by randomly sampling the pdfs of D_{void}, AR and θ. These points are further selected at P_s values ranging from 5 to 15 GPa at 1 GPa intervals to obtain a total of 10^7 points. The values of $\tau_{critical}$ at these sampled 10^7 MC points are obtained by probing the hypersurface and used to compute the median and 95% confidence intervals for $\tau_{critical}$. In the current work, this procedure is repeated to construct the median and 95% confidence intervals of $\tau_{critical}$ at the 10 discrete values of P_s, yielding the criticality envelope for class V and R10 pressed HMX materials. The procedure is followed to obtain the criticality envelope for the three reaction chemistry models.

III. RESULTS AND DISCUSSION

The three chemical kinetics models, H1, M1, and T3, are used in this work to compare their effects on the mesoscale response of

a pressed HMX material. In the multi-scale workflow shown in Fig. 1, high fidelity void collapse calculations are performed to obtain the ignition and growth rates of hotspots. Data from a sufficiently large ensemble of void collapse simulations are used to construct the surrogate model using the algorithm described in Sen *et al.*[61] The hotspot evolution data, as described in Sec. II, are employed to construct meso-informed surrogate models of the ignition and growth rates $\dot{F}_{ignition}$ and $\dot{F}_{growth}$; macro-scale reaction progress is then calculated by solving Eq. (27). Sixty void collapse simulations for each chemical reaction model were found to provide a surrogate model with an out-of-bag[62] RMSE of ∼0.5%. 1D macro-scale computations are then performed to compare the critical energy required for shock-to-detonation transition, as shown in Eq. (28). The following sections describe the computational results and insights obtained from the calculations.

A. Effects of reaction kinetics models on hotspot ignition and growth

First, to understand the peculiarities of the three reaction models, we compare their effects in two standard settings:

(1) Tarver *et al.*'s classical critical hotspot analysis[12] is performed to develop a hotspot criticality curve. This is done using 2D reaction-diffusion calculations as in Tarver *et al.*, where a circular hotspot of a given diameter D_{hs} and uniform temperature T_{hs} is initially placed in the center of a square domain. The reaction-diffusion calculations determine whether the hotspot grows or dissipates over time, thus defining the envelope of criticality in the (D_{hs}, T_{hs}) space.

(2) We then perform reactive void collapse simulations utilizing the setup shown in Fig. 3(a). In this second type of calculations, the ignition and growth of hotspots are tracked and hotspot criticality is identified as the condition where the resulting non-circular hotspot grows into a steady deflagration front. Since the void collapse-generated hotspot intensity and shape depends on the shock strength this second criticality criterion in the (D_{void}, P_s) space is more relevant to shock sensitivity than the Tarver critical hotspot criterion.

1. Tarver criticality: Reaction-diffusion calculations of hotspots

To estimate critical conditions for hotspot ignition and sustained growth, Tarver *et al.*[12] performed reaction-diffusion calculations using the three-equation (T3) reaction kinetics model for HMX, Eqs. (12)–(14). The critical hotspot curve in Fig. 6 was obtained by instantaneously heating the hotspot of a certain diameter D_{hs} to a specified temperature T_{hs} while keeping the surrounding temperature at ambient conditions. Depending on the initial temperature and size of the hotspot, chemical reaction may be sustained and the hotspot may grow to consume the surrounding material (critical hotspot) or it may extinguished due to thermal diffusion (subcritical hotspot). Rai *et al.*[36] verified that the threshold curve obtained for the T3 model using the current SCIMITAR3D code was in good agreement with the Tarver *et al.* result for prediction of the criticality curve. Here, we compare the threshold curves for the three reaction models, H1, M1, and T3.

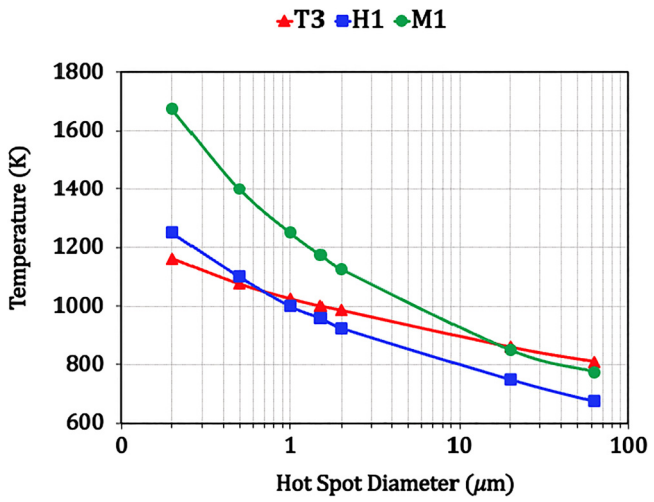

FIG. 6. Comparison of critical hot spot for HMX between three reaction models M1, T3 and H1. H1 is more sensitive for larger hotspot diameters. A crossover between T3 and H1 is observed at a hotspot diameter of 0.7 μm whereas M1 is insensitive compared to T3 and H1.

Figure 6 shows the comparison of the threshold curves for hotspot diameters ranging from 0.1 to 60 μm. Larger hotspots require lower temperatures for H1 compared to M1 and T3. For small hotspot diameters, the M1 model requires significantly higher temperatures to yield criticality. A cross over in behavior is observed for M1 and T3 at hotspot diameters of approximately 20 μm. Note that in the current work, the pressed HMX materials of interest (class V and R10, Fig. 2) have void sizes centered around 1 μm. In this range of hotspot sizes, the H1 and T3 models are quite similar in behavior while the M1 model is significantly less sensitive. For the smaller sizes of hotspots relevant to the microstructures of interest, i.e., ranging from 0.1 to 2.0 μm, a crossover is observed between H1 and T3 as well. T3 produces criticality at lower hotspot temperatures for hotspot sizes in the range of 0.1–0.7 μm, while H1 is more sensitive for hotspot sizes above 0.7 μm. Note that M1 remains highly insensitive compared to T3 and H1 for smaller hotspot sizes. While Fig. 6 indicates that the differences in criticality between the H1 and T3 models are rather subtle; these seemingly subtle differences will be shown below to become amplified when these two models are employed to make macro-scale shock sensitivity predictions.

2. Reactive void collapse

The Tarver criticality envelope discussed above assumes a pre-existing circular hotspot at uniform temperatures. Hotspots that develop in shocked HE materials, generally do not conform to these conditions [see Fig. 5(b)]. Typical hotspots can have distinctly non-circular, contorted shapes at inception and their criticality starting from such an initial state must be assessed. In this section we compare the evolution of the hotspot between the three reaction models by performing reactive collapse calculations for single

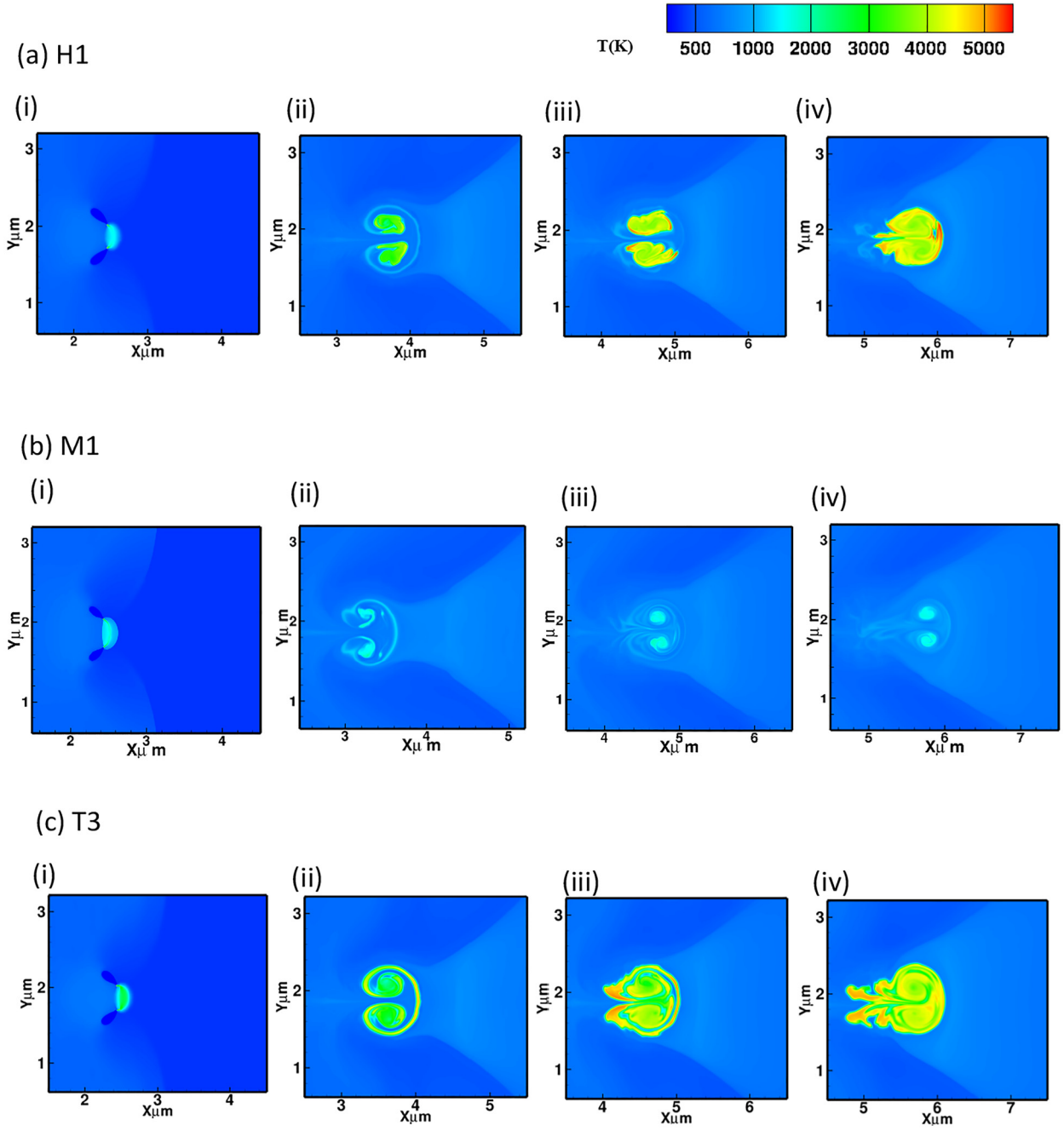

FIG. 7. Comparison of the hotspot temperature evolution with time for (a) H1, (b) M1 and (c) T3. The results are obtained from the reactive void collapse analysis of a single circular void of diameter $D_{void} = 1.2\ \mu m$ under shock load of pressure, $P_s = 13.5$ GPa. Multimedia available online.

circular voids as shown in Fig. 3(a). Reaction progress following void collapse is quantified by calculating the ignition and growth rates $\dot{F}^{scv}_{ignition}$, $\dot{F}^{scv}_{growth}$ using Eqs. (24a) and (24b). Various combinations of void diameters and shock pressure boundary conditions are employed to construct a criticality curve for void collapse-generated hotspots.

Figure 7 (Multimedia available online) shows a detailed comparison of reactive void collapse between the three reaction models

for a 1 μm void subjected to a shock of pressure $P_s = 13.5$ GPa. The temperature contours for hotspot evolution at four different time instances are shown in Fig. 7. Localization of energy due to void collapse alone, i.e., prior to the initiation of reactions, is independent of the reaction model for a given void diameter and shock load. Therefore, the initial stage of jet formation and void collapse is similar for all three reaction models, H1 [Fig. 7(a,i)], M1 [Fig. 7(b,i)], and T3 [Fig. 7(c,i)]. Following the collapse of the void, the second set of frames, i.e., Figs. 7(a,ii)–(c,ii), shows the effects of initiation of reaction for the different models. The reaction initiation for T3, (c,ii) is seen to be stronger compared to the other models. As observed in Rai *et al.*,[36] while the jet impact initiates a strong hotspot, this initial arc-shaped hotspot is drawn out into a thin cap structure due to vortical action centered at the secondary sidelobes formed due to jetting. This leads to the concentration of the hotspot reactions in the vortical roll-up region formed when the sidelobes collapse, as observed in the panels in the second column in Fig. 7. The concentration of the initiation event for the hotspot at the secondary lobe locations is strongest for T3 and weakest for the M1 model. Figure 7 shows that in contrast to H1 and T3, the reaction initiation for M1 is much weaker as there is no distinct hotspot formation. Note also that despite the rather subtle differences in the criticality behavior seen in Fig. 6(b), the H1 and T3 models produce noticeable differences in the shape and size of the hotspots in Figs. 7(a,iv) and 7(c,iv), respectively.

The third and fourth columns of temperature contour frames, i.e., Figs. 7(a–c,iii)–(a–c,iv), show the hotspot growth phase for the three models. For T3 [Fig. 7(c,iii)], the hotspot growth is nearly uniform along its periphery. The two distinct lobes formed at the reaction initiation stage grow into an approximately circular hotspot in the growth phase, aligning with the notion of the Tarver critical hotspot. The difference between the H1 and T3 is rather subtle. The hotspots for these two models appear to be quite similar. For H1, Fig. 7(a,iii), the overall temperatures in the hotspot are marginally lower compared to T3. Unlike T3, the H1 hotspot tends to grow predominantly from the secondary lobes formed during the reaction initiation. Eventually, in Fig. 7(a,iv), the sidelobe generated hotspots merge to form a near-circular Tarver-type critical hotspot. In contrast to H1 and T3, the M1 model displays low initiation sensitivity for the imposed shock strength and the hotspot begins to die off due to thermal diffusion. Figures 7(a,iv)–7(c,iv) display the final stages of hotspot growth, showing sustained growth of the hotspot in the cases of H1 and T3, but a weakening of the hotspot toward extinction in the case of M1. In this case, the T3 hotspot is marginally more intense than the H1 hotspot at the same time instant, signifying a faster hotspot growth rate for T3. However, the differences between H1 and T3 for the case shown are quite modest.

Figure 8 compares the time evolution of key hotspot QoIs for the surrogate model construction in the multiscale calculations to follow. The QoIs plotted are the area of void [Fig. 8(a)], area of hotspot [Fig. 8(b)], temperature of hotspot [Fig. 8(c)], and the product mass fraction [Fig. 8(d)]. These plots provide insights into the sensitivity of hotspot evolution to the reaction kinetics models. Figure 8(a) shows that the void collapse process (quantified by the area of the void vs time) is independent of the reaction kinetic models; this is expected, as the collapse time is too short for the effect of temperature rise due to chemical reactions to influence the strength of the material during the void collapse. However, as seen in Fig. 8(b), the area of the hotspot initiated after collapse is significantly different for M1 when compared to the other two models. Figure 8(c) shows that the temperatures reached at the instant of collapse and in the early growth phase (starting from times of about 0.6 ns) are quite similar for the H1 and M1 models. However, counterintuitively, as seen in Fig. 8(d), the evolution of the hotspots, quantified using the calculated value of the reaction product fraction F [Eq. (22)], is quite different between the two models H1 and M1. The H1 model produces a steadily growing hotspot while the M1 hotspot fails to grow. This difference in the trajectory of the hotspots between these two models stems from the difference in their Arrhenius reaction rate parameters (see Table II); as seen in Figs. 8(b) and 8(c) the initial temperature and area of the H1 and M1 hotspots are not very different; however, the subsequent growth of the reaction is higher for H1 than for M1, leading to a critical hotspot in the case of H1 but not for M1. This difference is consistent with the concept of the Tarver critical hotspot; an initial hotspot of a certain size and temperature will grow into a sustained steady deflagration front if the energy released by chemical reactions can overcome thermal diffusion.

In summary, for a given void size and loading condition, the hotspots arising from the different reaction models can vary subtly in shape, size, and intensity. The key question is: to what extent do these variations (for example, the subtle difference between H1 and T3) in the hotspot behavior influence the macro-scale shock-to-detonation phenomena in a multiscale calculation?

3. Effect of reaction chemistry on surrogate models for $\dot{F}_{ignition}$ and $\dot{F}_{growth}$

Ensembles of high-fidelity void collapse computations are performed to construct the surrogates for $\dot{F}_{ignition}$ and $\dot{F}_{growth}$ for the three reaction models using the procedure described in Sec. II D. These surrogate models provide the bridge between the meso- and macro-scale as shown in Fig. 1(e).

To construct the surrogates for use in predicting the shock sensitivity of class V and R10 microstructures, the void diameter range was chosen to be between 0.1 and 5 μm and calculations were performed for imposed shock pressure between 5 and 25 GPa. Figure 9 shows the surrogate models constructed using the three reaction models. The $\dot{F}_{ignition}$ hypersurfaces are shown in Figs. 9(a)(i)–9(c)(i), i.e., in the left column, while the $\dot{F}_{growth}$ hypersurfaces are shown in Figs. 9(a)(ii)–9(c)(ii), i.e., in the right column.

The ignition and growth hypersurfaces provide a comprehensive picture of the variations in the hotspot evolution for the different reaction rates. Several notable differences in behavior of the hotspots are indicated by the hypersurfaces in Fig. 9. Overall, it is straightforward to see that the M1 model in Fig. 9(b)(i,ii) provides ignition and growth rates much lower than the other two models, over the entire range of void diameters and pressures studied. It is also observed that the magnitudes as well as topology of the hypersurfaces for the three reaction models are quite different. Figure 9(c)(i,ii) shows the hypersurfaces for the T3 model; the $\dot{F}_{ignition}$ surface displays a gradual increase with pressure but insensitivity to the void diameter. Figure 9(a)(i,ii) shows that with the

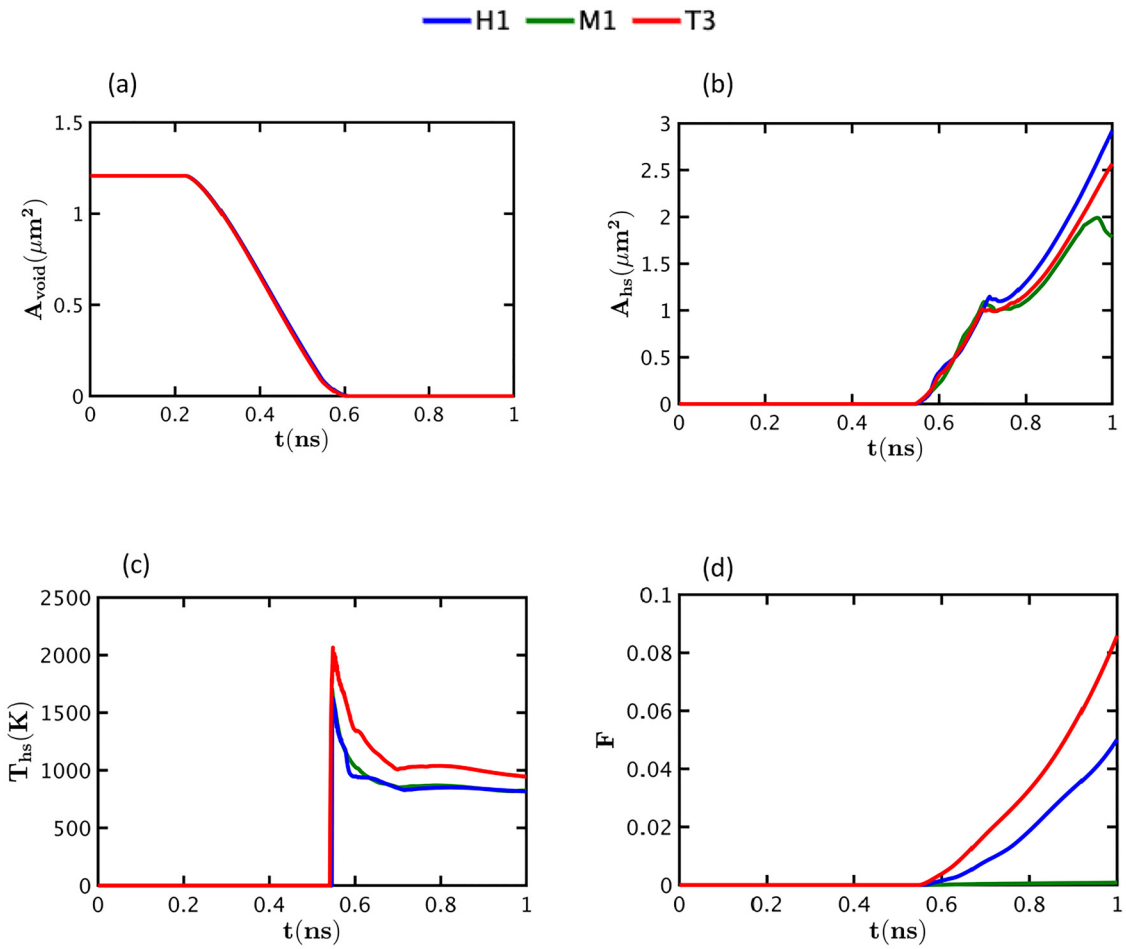

FIG. 8. Comparison between H1, M1, and T3 models for reactive void collapse analysis of a single circular void of diameter $D_{void} = 1.2\ \mu m$ under shock load of pressure, $P_s = 13.5$ GPa. The figures show the variation with time of (a) void area, (b) hotspot area, (c) average hotspot temperature, and (d) the product mass fraction F.

H1 model the $\dot{F}_{ignition}$ values are lower than T3 for small void diameters and low pressures. However, for higher pressures and larger void diameters, the ignition rates for H1 are higher than those of T3. This behavior was also seen in the reaction-diffusion calculation in Sec. III A 1, where H1 provided higher sensitivity for larger hotspot diameters relative to the T3 model. The reason behind the modest variation of $\dot{F}_{ignition}$ for T3 with pressure and void size is the moderating influence of intermediate steps in the decomposition of HMX, where the first step is endothermic, and the second step is mildly exothermic. The final step of the decomposition of HMX fragments into product gases releases the bulk of the chemical energy. The multi-step nature of the T3 model makes its response to loading more complex than that of the one-equation models, as described in detail by Rai *et al.*[36] The higher values of $\dot{F}_{ignition}$ in the peak region of the hypersurface for H1 are due to the single-step decomposition mechanism which requires stronger loading conditions to initiate chemical reactions. In contrast to T3 and H1, the $\dot{F}_{ignition}$ hypersurface in Fig. 9(b)(i) for M1 shows that this chemical reaction model is relatively insensitive to the shock across the range of pressures and void sizes. Note that Menikoff[42] calibrated (decreased) the value of the collision frequency Z to match macro-scale 1D shock propagation data for PBX 9501. When applied to the meso-scale hotspot calculations, this low value of Z (relative to H1) renders the M1 model sluggish in its energy release rate.

The $\dot{F}_{growth}$ hypersurfaces for the three models are shown in Figs. 9(a)(ii)–9(c)(ii). The M1 model in Fig. 9(b)(ii) shows only modest reaction initiation and growth only at larger void sizes and high pressures. For T3, Fig. 9(c)(ii), the $\dot{F}_{growth}$ values increase with pressure. For H1, Fig. 9(a)(ii), the $\dot{F}_{growth}$ values are higher than T3 for pressures above 15 GPa. The noticeable difference between the T3 and H1 hypersurfaces for $\dot{F}_{growth}$ is the relatively complex topology of the T3 hypersurface, while the H1 hypersurface is monotonic along both the P_s and D_{void} axes. The H1 hypersurface, Fig. 9(a)(ii) shows a steep increase of $\dot{F}_{growth}$ at small void diameters and high pressures; whereas the T3 hypersurface in Fig. 9(c)(ii) shows a

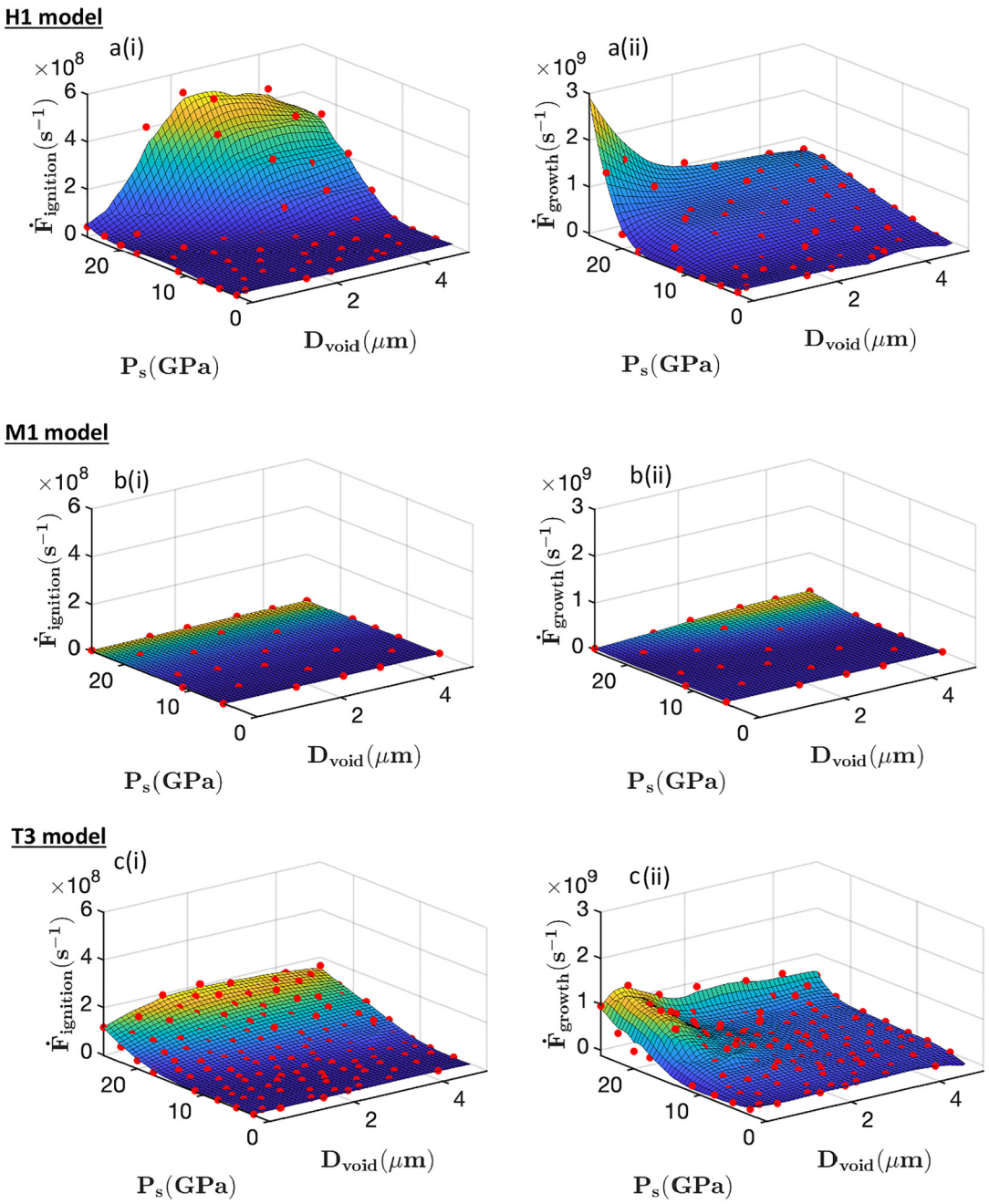

FIG. 9. Surrogate models constructed with respect to shock pressure P_s and void size D_{void} for the three reaction models $\dot{F}_{ignition}$ and $\dot{F}_{growth}$ for a[(i) and (ii)] H1, b[(i) and (ii)] M1 and c[(i) and (ii)] T3. The red dots pertain to the locations where highly resolved void collapse computations were performed. The hypersurfaces shown are fit to the input data (red dot) points by the Kriging algorithm.

saturation of the $\dot{F}_{growth}$ values as the pressure increases. In addition, both the H1 and T3 hypersurfaces are nearly flat along the D_{void} axis for lower pressures indicating that the growth rate of hotspots is relatively insensitive to the void size for low pressures, i.e., below 15 GPa. However, while H3 provides a steep increase in the hotspot growth rates at small void sizes for pressures higher than 15 GPa, the T3 model shows a more complex non-monotonic trend. In fact, the growth rates decrease for small voids in the T3 model; there is

an optimal void diameter of about 1 μm for the hotspot growth rate in the T3 model.

To further distinguish the above differences in the hotspot ignition and growth behavior exhibited by the three models, Fig. 10 shows normalized difference hypersurfaces for $\dot{F}_{ignition}$ and $\dot{F}_{growth}$, plotted in the form of contours in the (D_{void}, P_s) space. These difference hypersurfaces are calculated by treating the T3 hypersurface as the reference and taking the difference between the H1 and M1 hypersurfaces relative to the T3 hypersurface. The normalization is done by dividing the difference by the mean value of the T3 hypersurface; for example, for the difference hypersurface of H1, $\delta\dot{F}^{H1} = (\dot{F}^{H1} - \dot{F}^{T3})/\overline{|\dot{F}^{T3}|}$. Figures 10(a) and 10(b) show that the energy deposition rate for T3 is higher than H1 for pressures below 15 GPa. $\dot{F}_{ignition}$ values for H1 are higher than that of T3 for $P_s > 15$ Gpa and $D_{void} > 2$ μm and lower than T3 for small void diameters, i.e., $D_{void} < 1$ μm. The $\dot{F}_{growth}$ difference hypersurface for H1 shows that for $P_s > 20$ GPa, the hotspot growth rates for H1 are higher than those of T3. For void diameters $D_{void} > 2$ μm and pressures higher than 10 GPa, energy localization for H1 is greater than that of T3. Therefore, the crossover between H1 and T3 shown in the Tarver critical hotspot space in Fig. 6 translates into the differences in sensitivity embedded in the $\dot{F}_{ignition}$ and $\dot{F}_{growth}$ hypersurfaces. These differences will further be transmitted to the macro-scale closure model and influence the overall shock sensitivity predictions made with the reaction chemistry models. Figures 10(c) and 10(d) show that the energy deposition rate for M1 is lower than T3 throughout the pressure and void diameter range.

In summary, the above analysis shows that the energy localization at hotspots is impacted in different ways by the reaction chemistry model. While the M1 model remains rather tepid in its effects across the entire range of void sizes and pressures examined in this study, the H1 and T3 models exhibit sensitivity to the void size, but in different ways, as the shock strength is increased. The surrogate models in Fig. 9 encapsulate and help visualize the subtleties in the differences between the reaction chemistry models and their coupling with the mechanics of void collapse. At this stage, the question is: how do these subtle differences in the hotspot energy deposition rates produced by the three models upscale to influence the macroscale shock sensitivity?

B. Macro-scale effects of reaction kinetics models

1. Microstructure quantification: Statistical description of the morphology of void fields

Welle *et al.*'s[8,37] experiments on neat-pressed HMX showed that shock sensitivity, as determined by the critical energy for initiation, is strongly dependent on the microstructural features of the void network in the material. Two different classes of pressed HMX material microstructures are analyzed in this work, class V and R10, whose microstructures are depicted in Fig. 2. These microstructures differ substantially in the overall porosity value ($\phi = 14\%$ and 7%, respectively), while the differences in the D_{void}, AR, θ, ϕ are rather modest. A meso-informed predictive model for the sensitivity of these two classes of materials must relate the microstructural morphology to the observed macroscopic response. In this section, we employ the hotspot ignition and growth surrogates developed at the meso-scale to examine how the interplay between meso-scale hotspots and microstructure influence the macro-scale shock sensitivity in the James[38]/Walker–Wasley[54] space.

First, the microstructural features are quantified through pdfs of D_{void}, AR, θ. Detailed descriptions of the techniques for computing the morphological descriptors are provided in the previous work by Roy *et al.*[14] Using the techniques in Roy *et al.*, we obtain: (1) D_{void}, the effective diameter of the voids in the material, which is calculated for each void in the sample from $A_{void} = \pi D_{void}^2/4$, i.e., by calculating an effective diameter of a circular void of the same area as the arbitrary-shaped void; (2) AR, the aspect ratio of the voids, calculated from the ratio of length of the longest intercept within the pore to the intercept perpendicular to it; (3) θ, the orientation of the major axis of the void relative to the incoming shock, computed under the assumption that the material is loaded from the west face of the sample; and (4) ϕ, the overall porosity of the material. These four parameters are quantified from subsamples of scanning electron micrographs for the two classes of pressed HMX shown in Figs. 2(a) and 2(b).

Probability density functions (pdfs) for the parameters D_{void}, AR, θ are calculated for each class of material. Figures 2(c)–2(e) show the pdfs for D_{void}, AR, θ for class V (red) and R10 (blue) HMX materials. The pdf of D_{void} in Fig. 2(c) for the R10 microstructure shows high probability densities in the range of $0.1 < D_{void} < 3.0$ μm. The class V microstructure shows higher probability densities for $0.1 < D_{void} < 3.4$ μm. Thus, the void sizes in the two classes of materials are quite similar. The pdf of AR for R10 in Fig. 2(d) shows a peak at AR = 6.5, with aspect ratios of voids ranging from $2 < AR < 10$, while the AR pdf for class V has a peak at AR = 5.8, with aspect ratios of voids ranging from $2 < AR < 7.5$. The pdf for the void orientation θ for both the materials shows a multimodal distribution in Fig. 2(e). Therefore, these two classes of HMX are quite similar in their microstructures, with some noticeable but modest shifts in the distributions of the void characteristics. The final global morphological parameter is the porosity ϕ which is calculated by summing the area occupied by the voids in the domain and normalizing by the area of the sub-sample. The calculated average porosity for the R10 microstructure is $\phi = 7\%$ and for class V is $\phi = 14.5\%$. This difference can be viewed in the sub-sample images of R10 and class V [Figs. 2(a) and 2(b)]. Thus, in terms of the microstructural morphology, the strongest difference between the two microstructures is in terms of the porosity value, with class V having a higher value of porosity than R10.

2. Macro-scale simulations of SDT in pressed HMX

Macroscale computations of SDT are performed on a 1D coupon of solid HMX materials as shown in Fig. 3(b). The material is loaded with a shock pulse of pressure P_s and duration τ_s at the west boundary of the coupon. The shock propagates through the coupon from left to right. 400 grid points were used across the 1D domain, based on grid sensitivity studies to establish convergence of the calculated pressure profiles.[43] The coupon is loaded for

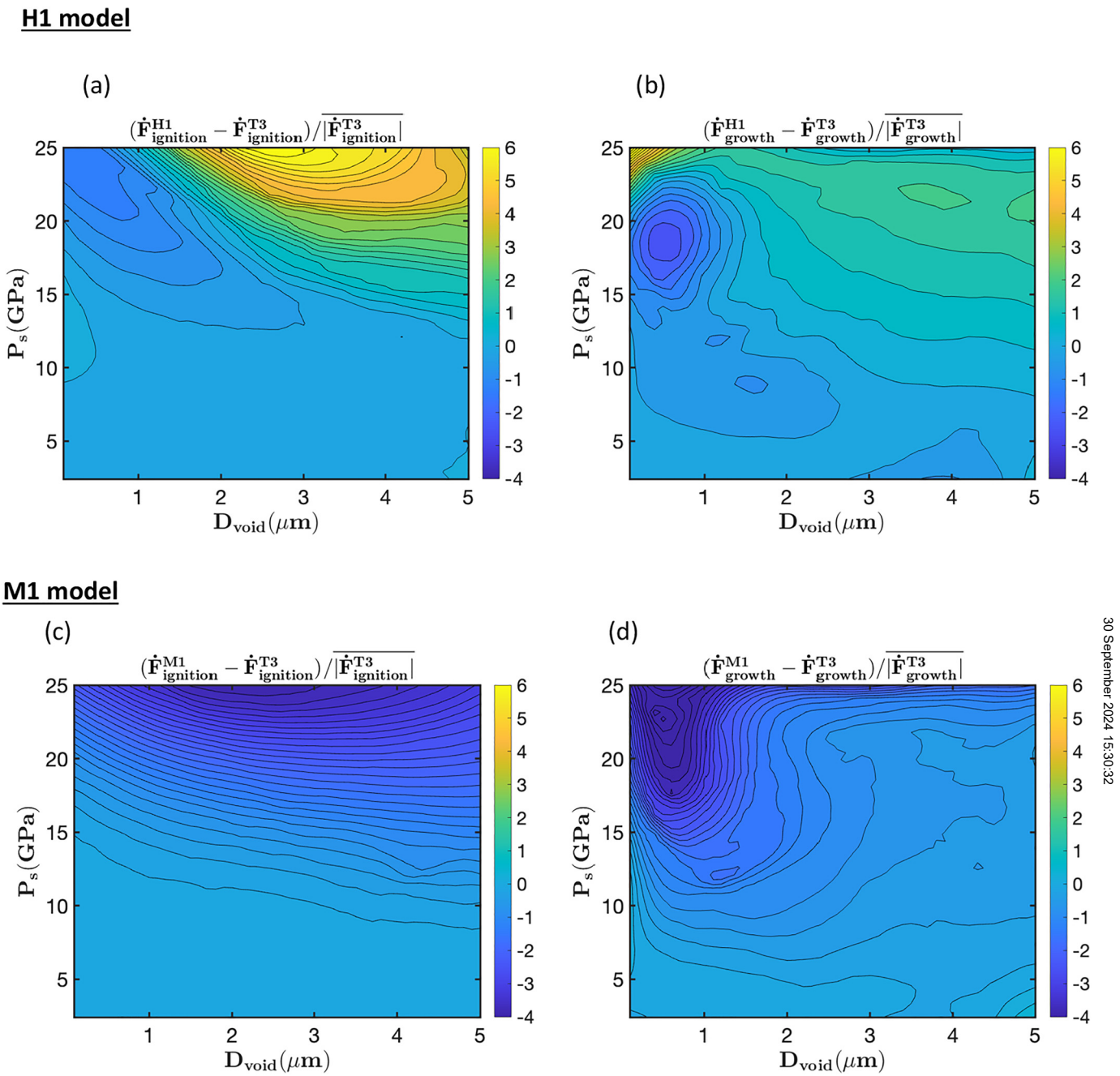

FIG. 10. Normalized difference hypersurface (a) and (c) $\dot{F}_{ignition}$ and (b) and (d) $\dot{F}_{growth}$ for M1 and H1 with respect to T3. The difference fields in the figures are shown with 25 levels of contour lines.

various combinations of P_s and τ_s. In the MES-IG model, the energy localization at the mesoscale is passed to the macroscale through the surrogate models for $\dot{F}_{ignition}$ and $\dot{F}_{growth}$. At each grid point, the meso-scale energy deposition rate is supplied as a function of the shock pressure and the underlying (unresolved, homogenized) microstructural parameters (D_{void}, AR, θ, and ϕ). The local pressure is tracked over time in each 1D control volume as described in Sec. II D 1, to determine the advent of SDT, i.e., the time instant when the pressure at a grid point reaches the value of the von-Neumann spike pressure. The criticality curve is

constructed by computing $\tau_{critical}$ for each combination of P_s, D_{void}, AR, θ, and ϕ as described in Sec. II D 2. These calculations to construct the criticality curve are performed for the three reaction chemistry models (H1, M1, and T3) and the two classes of pressed HMX (class V and R10).

To understand how the predictions of SDT differ for the different reaction kinetic models and microstructures, we plot the pressure profiles in the coupon at equal intervals of time, starting from the initial shock state to the final steady detonation state. The evolution of pressure along the coupon is shown for the R10 microstructure at two shock pressures, $P_s = 9.5$ and 13.5 GPa, for different shock pulse durations. The microstructural parameters are fixed for all the computations at $D_{void} = 1\,\mu m$; $AR = 1$; $\theta = 10°$, and $\phi = 7\%$. Figure 11(a) shows that for $P_s = 9.5$ GPa and shock pulse duration $\tau_s = 7$ ns, the incident shock is eventually dissipated by the reflected rarefaction front for all three reaction models. For a higher shock pulse width [Fig. 11(b)], $\tau_s = 9$ ns, the shock builds to a steady detonation wave for the T3 model, while build-up to detonation is suppressed for H1 and M1. When the shock pulse duration is further increased to $\tau_s = 15$ ns [Fig. 11(c)], both T3 and H1 models provide SDT. This indicates that for a 1 μm void and 9.5 GPa pressure, T3 leads to detonation faster compared to H1 and M1. This is due to higher energy deposition at the mesoscale for T3 for smaller diameters and lower pressures, as indicated in the criticality curve shown in Fig. 6 and in the hypersurfaces shown in Fig. 9. When the pressure is increased to $P_s = 13.5$ GPa in Fig. 11(d), T3 and H1 show similar SDT behaviors for the shock pulse duration of 7 ns, whereas the shock fails to transition to detonation even for this high pressure for M1. In fact, the M1 model is seen to be highly insensitive and the low values of $\dot{F}_{ignition}$ and for $\dot{F}_{growth}$ in Fig. 9(a) lead to a model that does not produce SDT for values that are reasonably close to experimentally determined criticality envelopes for class V.[37]

Figure 2(c) shows that, for class V and R10 microstructures, the void diameters are centered around 1 μm. The energy

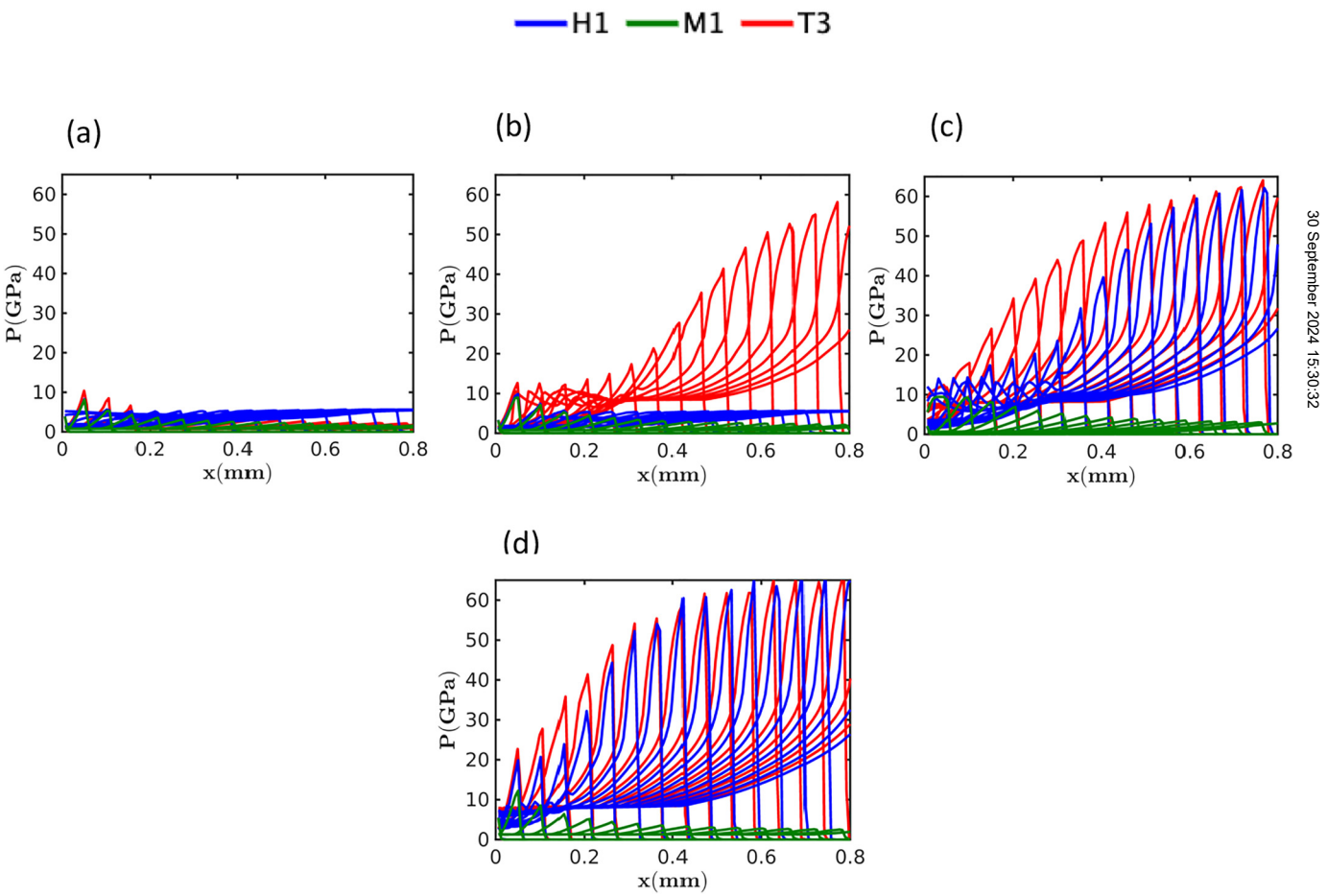

FIG. 11. Pressure evolution in macroscale computations for the R10 material microstructure subjected to a shock pressure of 9.5 GPa, and for shock pulse duration (a) $\tau_s = 7.0$ ns (b) $\tau_s = 9.0$ ns (c) $\tau_s = 15.0$ ns. (d) Pressure evolution in macroscale computations for the R10 material subjected to a shock pressure of 13.5 GPa for shock pulse duration, $\tau_s = 7.0$ ns. For all the computations AR = 1, $\theta = 20°$ and void volume fraction $\phi = 7\%$.

deposition hypersurfaces in Fig. 9 show that for such void sizes, H1 and T3 provide sufficiently high $\dot{F}_{ignition}$ and for $\dot{F}_{growth}$ values as P_s increases, while the response from M1 remains weaker than the other two models. The following section compares the predictions of the models with experimental criticality curves, further emphasizing that the M1 model is not well suited for meso-scale calculations of hotspot evolution.

3. Comparison of criticality (Walker–Wasley) curves

To compare the sensitivity predictions from the reaction models, the criticality or go-no-go envelopes (Walker–Wasley curves plotted in the P–τ_s space, where P is the shock pressure and τ_s is the shock pulse duration) were computed for both class V and R10 pressed HMX materials. To obtain the criticality (go-no-go) envelope, 1D macroscale computations were performed for input shock pressures ranging from 4 to 16 GPa and for a range of shock pulse durations. As noted in the previous section, due to the low energy deposition rates at the mesoscale, the M1 model does not produce macroscale SDT for the entire range of shock pulse durations $0 < \tau_s < 50$ ns. Therefore, this section only presents the macroscale sensitivity behaviors for two reaction models, H1 and T3.

Figure 12(a) shows the comparison of the criticality envelopes for the class V material for H1 and T3 with the experimental data of Molek *et al.*[37] Both T3 and H1 show good agreement with the experiments. For the small void diameters centered around 1 μm in size, T3 is more sensitive compared to H1, and the criticality envelope from T3 agrees well with the experimental data over the entire range of pressures and pulse durations. For pressures above 13.5 GPa, T3 and H1 are in close agreement. As the pressure decreases H1 diverges from T3, particularly in the elbow region of the criticality curve. In Sec. III A 3, it was shown that for lower pressures the energy deposition rate for T3 is higher than that for H1, which is reflected in the separation of the criticality envelopes between the two models in the elbow of the curve.

The sensitivity predictions between the two reaction models vary with the material microstructure. Figure 12(b) shows the criticality curves for the R10 microstructure which has a lower porosity ($\phi = 7\%$) compared to class V ($\phi = 14.5\%$). Unfortunately, experimental data for R10 do not exist in the open literature; therefore, the good agreement seen in the above class V predictions using the current model must be relied on to provide confidence in the R10 analysis. R10 criticality predictions with the H1 and T3 models show similar behavior for pressures above 10 GPa. For pressures below 10 GPa, H1 is seen to be less sensitive than T3; the difference between H1 and T3 is greater for R10 than for the class V microstructure. As the porosity of the material is lower, the critical energy required for SDT increases. The less sensitive H1 model therefore struggles to provide sufficient energy deposition rates at lower pressured and therefore deviates significantly from the T3 curve. Furthermore, despite the close similarity between class V and R10 microstructures in their void characteristics (as seen in the pdfs of Fig. 2), the porosity plays a significant role and the criticality curves for R10 are pushed up and to the right relative to class V.

Figure 13 provides insights into the subtle influence of the coupling between reaction chemistry models and microstructure on the meso-scale energy deposition rates, and their combined impact on macro-scale sensitivity. The figures display the pdfs of the hotspot growth rates $\dot{F}_{growth}$ for the class V microstructures at two different pressures, $P_s = 9.5$ GPa [Fig. 13(a)] and $P_s = 13.5$ GPa [Fig. 13(b)]. These pressure values can be seen in Fig. 12 to correspond to the elbow and asymptotic regions of the criticality envelope, respectively. There are distinct differences in the pdfs of the growth rates between the two reaction chemistry models. At the

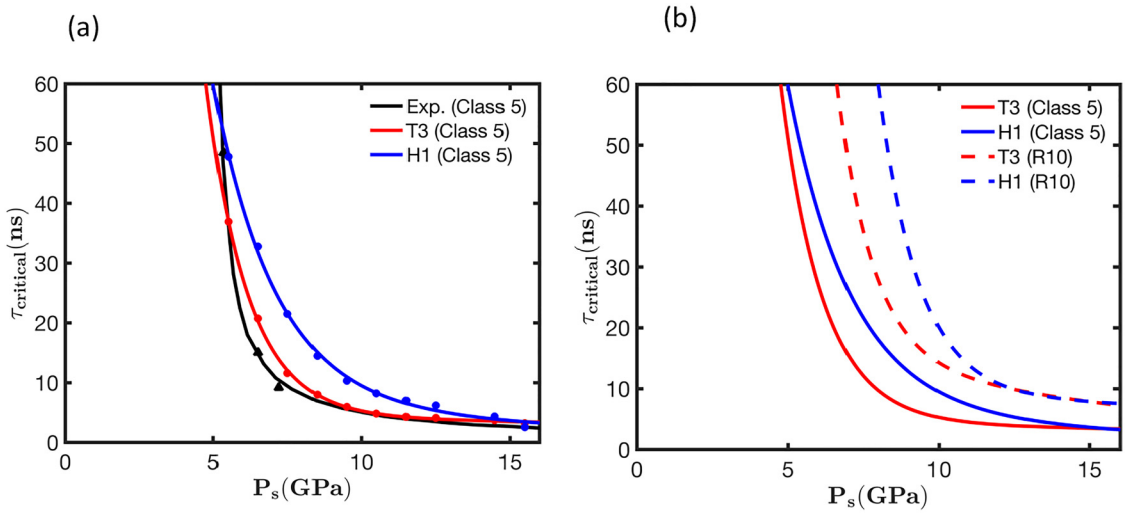

FIG. 12. Sensitivity predictions in the form of Walker–Wasley curves for (a) Class V material showing experimental data (black), H1 model predictions (blue), and T3 model predictions (red); M1 model predictions were outside of the space shown and are therefore not depicted. (b) Comparison of criticality curves between the two classes of HMX materials Class V and R10.

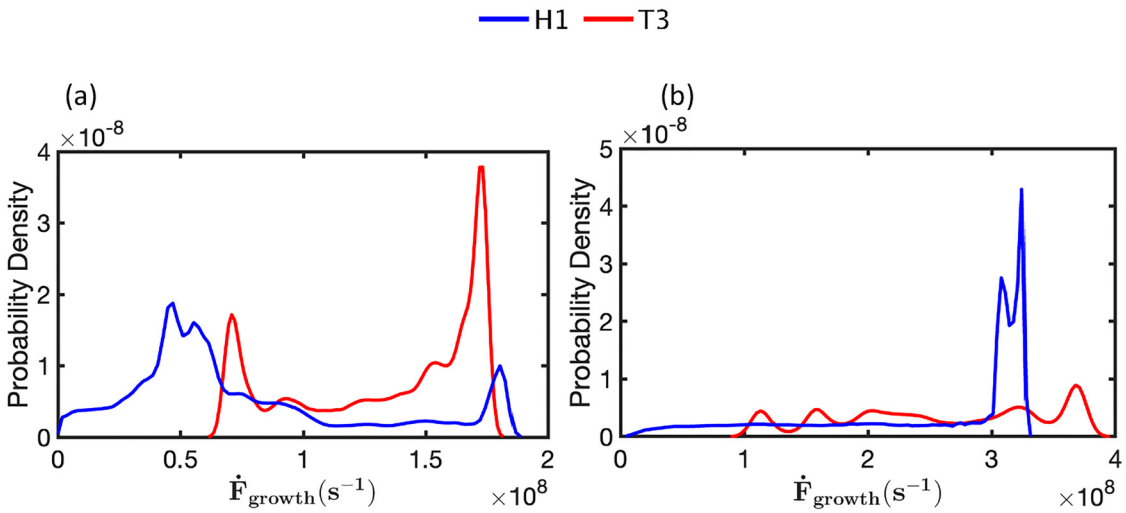

FIG. 13. Probability density distributions for $\dot{F}_{growth}$ for Class V microstructure for (a) 9.5 GPa and (b) 13.5 GPa. The median of the distribution is higher for T3 compared to H1 at 9.5 GPa whereas for higher pressures the median value of H1 is higher.

lower pressure, P = 9.5 GPa, the pdfs for both reaction chemistry models display a bimodal structure; however, the T3 model shifts the pdf of $\dot{F}_{growth}$ to the right, implying a higher sensitivity than the H1 model. At the higher pressure [Fig. 13(b)], the pdfs of the two models show distributions that are very different in profile; in this case, the H1 model shows a distinct peak in the $\dot{F}_{growth}$ distribution whereas the T3 model has a relatively flat profile. However, the medians of the distribution are relatively close to each other. The differences between the two models seen in Fig. 13(b) do not lead to significant differences in the predicted criticality envelope (Fig. 12). At the higher pressure, the hotspot growth rates are large enough to drive the shock to detonation even for short pulse widths. In the elbow region, however, i.e., at the lower pressure of 9.5 GPa, the magnitudes of $\dot{F}_{growth}$ are lower [Fig. 13(a)] and the differences between the two models can cause significant separation in their criticality envelopes.

The key point to note, through the stages of the multi-scale model in the above sections, is that subtle differences in the energy delivery rates due to the reaction kinetic models, beginning with those noted in the Tarver criticality curve in Fig. 6(b), propagate to the meso-scale dynamics represented by the surrogate models in Fig. 9, and impact the overall macro-scale shock sensitivity in Fig. 12. The influence of the reaction chemistry models is the strongest in the threshold region in the Walker–Wasley/James space, i.e., in the elbow region of the criticality envelope shown in Fig. 12. This is consistent with intuition as it is expected that reaction chemistry as well as microstructures are likely to play the strongest role in determining the threshold conditions for initiation.

IV. CONCLUSIONS

In a multi-scale predictive framework, models for reaction rates expressed in Arrhenius forms are key to calculations of hotspot ignition, growth and thereby for the construction of closure (reactive burn) models. However, even for a commonly used energetic material (e.g., HMX in this paper), there are a wide variety of reaction rate models available, and it is not clear which model accurately represents the reactive response of the material. Of all the reaction chemistry models available for HMX, three global models, namely, the Henson one-equations, Menikoff one-equation, and Tarver three-equation models are commonly used to represent HMX decomposition under various initiation conditions. Hitherto, it has not been possible to establish which, if any, of these three models should be chosen to represent energy localization and reactive dynamics in meso-scale simulations. This is because, in practice, the sensitivity of an energetic material such as HMX is determined in macro-scale experiments. Establishing which reaction model to use is dictated by a "top-down" analysis guided by macro-scale experiments. In this work, we started with experimentally measured macro-scale sensitivity results for a class V pressed HMX material and examined which reaction models produce the best agreement with the experimental sensitivity curves. In other words, here the ground truth for the assessment is taken to be the ability of the models to best match the criticality/go-no-go envelope[37,59] for a pressed HMX material. The three models, H1, M1, and T3, were employed in a meso-informed ignition and growth model (MES-IG) which allows for connecting meso-scale hotspot dynamics to macro-scale SDT analysis.

Meso-scale calculations show that for a given void size and loading condition, the hotspot evolution arising from the different reaction models varies, both in the shape, size, and intensity of hotspots. Therefore, energy localization at hotspots is highly sensitive to the reaction chemistry model. The reaction models provide different energy localization rates as the shock pressures and void diameters are varied. While the M1 model remains rather tepid in its effects across the range of void sizes and pressures, the H1 and

T3 models show higher sensitivity to the void size, but in different ways, as the shock strength is increased. These effects of the reaction rate models on energy localization rates carry through to the predicted macro-scale response of the pressed energetic materials. Based on the multi-scale model predictions of macro-scale criticality (Walker–Wasley/James envelope), we conclude that the H1 and T3 models are suitable for modeling the reactive dynamics of HMX. The M1 model on the other hand is rather insensitive and is not recommended. Among the H1 and T3 models, the subtle differences in the energy delivery rates due to the reaction kinetic models, beginning with those noted in the Tarver criticality curve, propagate to the meso-scale dynamics represented by the surrogate models for hotspot ignition and growth rates, and impact the overall shock sensitivity of the material. The influence of the reaction chemistry models is the strongest in the threshold region in the Walker–Wasley/James space, i.e., in the elbow region of the criticality envelope, whereas the model predictions approach each other at high shock pressures.

The multi-scale model with the H1 and T3 chemistry models predicted well the experimentally determined criticality envelope for pressed HMX class V microstructures. These results provide a guideline for model developers on the plausible range of time-to-ignition that are produced by physically correct Arrhenius rate models for HMX; the present study indicates that the reaction chemistry models for HMX lie in the time-to-reaction range of the Tarver-three equation and Henson global one-equation reaction models. This conclusion is subject to the caveat that the remaining crucial aspects of the models for HMX, namely, the thermophysical models (equation of state, mixture treatment, specific heat, and thermal diffusion, melt curve) and mechanical models (elasto-plastic deformation) and their coupling, are correctly represented in meso-scale calculations. Further work is underway to refine the thermo-mechanical models and properties of HMX in concert with the reaction chemistry models to arrive at a reliable model for the material.

ACKNOWLEDGMENTS

The authors gratefully acknowledge financial support from the Air Force Research Laboratory Munitions Directorate (AFRL/RWML), Eglin AFB, under Contract No. FA8651-16-1-0005 (Program manager: Dr. D. Barrett Hardin). Portions of this work are based upon work supported by the Air Force Office of Scientific Research under Award Nos. FA9550-15RWCOR123 and FA955018-18RWCOR108. We thank Dr. Jim Vitarelli and Mr. Matthew Stuthers for generating the scanning electron microscope data for the pressed HMX samples and Mr. Michael Meadows for his assistance in threshold studies.

AUTHOR DECLARATIONS

Conflict of Interest

The authors have no conflicts to disclose.

Author Contributions

P. Parepalli: Data curation (equal); Formal analysis (equal); Investigation (equal); Validation (equal); Visualization (equal); Writing – original draft (equal). **Yen T. Nguyen:** Data curation (equal); Formal analysis (equal); Investigation (equal). **O. Sen:** Methodology (equal); Software (equal). **D. B. Hardin:** Funding acquisition (equal); Writing – review & editing (equal). **C. D. Molek:** Funding acquisition (equal); Resources (equal); Writing – review & editing (equal). **E. J. Welle:** Funding acquisition (equal); Resources (equal); Writing – review & editing (equal). **H. S. Udaykumar:** Conceptualization (equal); Funding acquisition (equal); Project administration (equal); Supervision (equal); Writing – original draft (equal); Writing – review & editing (equal).

DATA AVAILABILITY

The data that support the findings of this study are available from the corresponding author upon reasonable request.

APPENDIX: EQUATIONS OF STATE FOR THE GASEOUS PRODUCTS AND SOLID HMX AT THE MACROSCALE

For the gas phase, the Jones–Wilkins–Lee (JWL) equation of state is used where the specific internal energy of the gas is given by

$$e_g(\rho_g, T_g) = e_{kg}(\rho_g) + C_{vg}T_g, \tag{A1}$$

where C_{vg} is the specific heat at constant volume, T_g is the temperature of the product gases, and

$$e_{kg}(\rho_g) = \frac{A_g}{\rho_0 R_{1g}} e^{-R_{1g}\frac{\rho_0}{\rho_g}} + \frac{B_g}{\rho_0 R_{2g}} e^{-R_{2g}\frac{\rho_0}{\rho_g}} + c_{ek} + \frac{k}{\rho_0 \Gamma_{g0}} \left(\frac{\rho_g}{\rho_0}\right)^{-\Gamma_{g0}}, \tag{A2}$$

where ρ_g is the density of the gas and ρ_0 is a reference density. The gas-phase pressure, p_g, is a function of internal energy and density and is given by

$$p_g(\rho_g, e_g) = \rho_g \Gamma_{g0}(e_g - e_{kg}(\rho_g)) + p_{kg}(\rho_g), \tag{A3}$$

where Γ_{g0} is the Grüneisen coefficient and

$$p_{kg}(\rho_g) = -\frac{de_{kg}}{d\left(\frac{1}{\rho_g}\right)}. \tag{A4}$$

The constants in Eq. (A1) are obtained from

$$k = [P_{CJ} - p_{kg}(\rho_{CJ}) - \rho_{CJ}\Gamma_{g0}C_{vg}T_{CJ}]\left(\frac{\rho_0}{\rho_{CJ}}\right)^{\Gamma_{g0}+1}, \tag{A5}$$

$$e_{ek} = -\frac{A_g}{\rho_0 R_{1g}} e^{-R_{1g}\frac{\rho_0}{\rho_{CJ}}} - \frac{B_g}{\rho_0 R_{2g}} e^{-R_{2g}\frac{\rho_0}{\rho_{CJ}}} - (P_{CJ} - p_{kg}(\rho_{CJ}))\frac{1}{\rho_{CJ}\Gamma_{g0}} + e_{CJ}, \tag{A6}$$

$$\frac{1}{\rho_{CJ}} = \frac{1}{\rho_0} - P_{CJ}\left(\frac{1}{\rho_0 D_{CJ}}\right)^2, \tag{A7}$$

TABLE IV. HMX parameters for the Cochran–Chan equation of state for the solid phase.

A_s (Pa)	B_s (Pa)	R_{1s}	R_{2s}	C_{vs}(J kg^{-1}K^{-1})	Γ_{s0}
1.287×10^{10}	1.342×10^{10}	4.1	3.1	1087	0.93

and

$$e_{CJ} = \frac{1}{2} P_{CJ} \left(\frac{1}{\rho_0} - \frac{1}{\rho_{CJ}} \right) + e_0. \tag{A8}$$

In Eqs. (A5)–(A8), P_{CJ}, T_{CJ}, ρ_{CJ}, e_{CJ}, and D_{CJ} are the pressure, temperature, density, specific internal energy, and the detonation speed at the CJ state, respectively, while e_0 is a reference specific internal energy.

For a solid phase, the Cochran–Chan equation of state is used to model the thermomechanical behavior of the solid under shocks. In this equation of state (EOS), the specific internal energy of the solid reactant is given by

$$e_s(\rho_s, T_s) = e_{ks}(\rho_s) + C_{vs} T_s, \tag{A9}$$

where C_{vs} is the specific heat at constant volume, T_s is the temperature of the solid, and

$$e_{ks}(\rho_s) = -\frac{A_s}{\rho_0 (1 - R_{1s})} \left[\left(\frac{\rho_0}{\rho_s} \right)^{1 - R_{1s}} - 1 \right] + \frac{B_s}{\rho_0 (1 - R_{2s})} \left[\left(\frac{\rho_0}{\rho_s} \right)^{1 - R_{2s}} - 1 \right] - C_{vs} T_0 + e_0, \tag{A10}$$

where ρ_s is the density of the solid phase and T_0 is the reference temperature. The solid pressure, p_s, is given by

$$p_s(\rho_s, e_s) = \rho_s \Gamma_{s0} (e_s - e_{ks}(\rho_s)) + p_{ks}(\rho_s), \tag{A11}$$

where Γ_{s0} is the Grüneisen coefficient and

$$p_{ks}(\rho_s) = \frac{de_{ks}}{d\left(\frac{1}{\rho_s}\right)}. \tag{A12}$$

The constants in the equations of state for the reactants and products are given in Tables IV–VI.

The products and reactants in the mixture in each macro-scale control volume are assumed to be in pressure and temperature

TABLE V. HMX parameters for the JWL equation of state for the product phase.

A_g (Pa)	B_g (Pa)	R_{1g}	R_{2g}	C_{vg}(J kg^{-1}K^{-1})	Γ_{g0}
12.18×10^{11}	12.3×10^{9}	4.766	1.102	815	0.408

TABLE VI. Variables at the CJ state and reference quantities for HMX.

P_{CJ} (Pa)	D_{CJ} (m/s)	T_{CJ} (K)	ρ_0(kg/m^3)	e_0(J kg^{-1})	T_0(K)
38.8×10^{9}	9300	4113.7	1905	0	298

equilibrium, i.e.,

$$p_s = p_g = p, \quad T_s = T_g = T, \tag{A13}$$

where p_s and T_s are the solid pressure and temperature and p_g and T_g are the pressure and temperature for the gas phase. The overall specific internal energy and the density for the control volume are also functions of the specific internal energy and density of the solid and gas phases,

$$e = (1 - \lambda) e_s + \lambda e_g \tag{A14}$$

and

$$\frac{1}{\rho} = \frac{1 - \lambda}{\rho_s} + \frac{\lambda}{\rho_g}, \tag{A15}$$

where e_s and ρ_s are the specific internal energy and the density for the solid phase and e_g and ρ_g are the specific internal energy and the density for the gas phase.

The equations of state for the solid and the gas phases can be combined with the above mixture laws [Eqs. (A13)–(A15)] to compute the pressure in the macro-scale control volume. The mixture law for the specific internal energy given by Eq. (A14), and the pressure equilibrium condition, in Eq. (A13) can be combined with Eqs. (A3) and (A11) to give

$$(1 - \lambda) \left(\frac{p - p_{ks}}{\rho_s \Gamma_{s0}} + e_{ks}(\rho_s) \right) + \lambda \left(\frac{p - p_{kg}}{\rho_g \Gamma_{g0}} + e_{kg}(\rho_g) \right) = e. \tag{A16}$$

Similarly, eliminating e_g from Eqs. (A1) and (A3) and e_s from Eqs. (A9) and (A11) in favor of T_s and T_g, the temperature equilibrium condition [Eq. (A13)] gives

$$\frac{p - p_{ks}(\rho_s)}{\rho_s \Gamma_{s0} C_{vs}} = \frac{p - p_{kg}(\rho_g)}{\rho_g \Gamma_{g0} C_{vg}}. \tag{A17}$$

Equations (A15)–(A17) provide three equations in terms of the mixture pressure p, and the densities of the gas and solid phases, ρ_g and ρ_s and can be solved simultaneously for a specified value of λ.

REFERENCES

[1]C. A. Handley, B. D. Lambourn, N. J. Whitworth, H. R. James, and W. J. Belfield, Appl. Phys. Rev. **5**, 011303 (2018).
[2]R. R. McGuire and C. M. Tarver, *Proceedings of Seventh International Symposium on Detonation* (1982), Vol. 82, p. 56.
[3]C. Gruau, D. Picart, R. Belmas, E. Bouton, F. Delmaire-Sizes, J. Sabatier, and H. Trumel, Int. J. Impact Eng. **36**, 537 (2009).

[4]B. Clements, "Merging the mechanical constitutive model viscoscram with the Henson-Smilowitz thermal ignition model to address weak-shock initiation," Report No. LA-UR-11-06289 (Los Alamos National Laboratory, 2011).
[5]S. Cochran and J. Chan, Lawrence Livermore Laboratory, pbx-9404, rx-03-bb, No.: UCID-18024 (1979).
[6]J. Zhang, T. L. Jackson, J. D. Buckmaster, and J. B. Freund, Combust. Flame **159**, 1769 (2012).
[7]S. Kim, C. Miller, Y. Horie, C. Molek, E. Welle, and M. Zhou, J. Appl. Phys. **120**, 115902 (2016).
[8]E. J. Welle, C. D. Molek, R. R. Wixom, and P. Samuels, J. Phys. Conf. Ser. **500**, 052049 (2014).
[9]A. Barua, Y. Horie, and M. Zhou, J. Appl. Phys. **111**, 054902 (2012).
[10]M. A. Wood, D. E. Kittell, C. D. Yarrington, and A. P. Thompson, Physi. Rev. B **97**, 014109 (2018).
[11]R. A. Austin, N. R. Barton, J. E. Reaugh, and L. E. Fried, J. Appl. Phys. **117**, 185902 (2015).
[12]C. M. Tarver, S. K. Chidester, and A. L. Nichols, J. Phys. Chem. **100**, 5794 (1996).
[13]R. Menikoff, AIP Conf. Proc. **706**, 393 (2004).
[14]S. Roy, O. Sen, N. K. Rai, M. Moon, E. Welle, C. Molek, K. K. Choi, and H. S. Udaykumar, Multiscale Multidiscip. Model., Exp. Des. **3**, 265 (2020).
[15]J. E. Field, N. K. Bourne, S. J. P. Palmer, S. M. Walley, and J. M. Smallwood, Philos. Trans. R. Soc. London **339**, 269 (1992).
[16]R. E. Winter and J. E. Field, Proc. R. Soc. London, Ser. A**343**, 399 (1975).
[17]J. P. Dear, J. E. Field, and A. J. Walton, Nature **332**, 505 (1988).
[18]F. Garcia, K. S. Vandersall, and C. M. Tarver, J. Phys. Conf. Ser. **500**, 052048 (2014).
[19]R. Menikoff, "Granular explosives and initiation sensitivity," Report No. LA-UR-99-6023 (Los Alamos National Laboratory, 1999).
[20]P. Das and H. Udaykumar, Shock Waves **32**, 593 (2022).
[21]S. Roy, B. P. Johnson, X. Zhou, Y. T. Nguyen, D. D. Dlott, and H. Udaykumar, J. Appl. Phys. **131**, 205901 (2022).
[22]L. Salvati, B. P. Johnson, W. P. Bassett, and D. D. Dlott, AIP Conf. Proc. **2272**, 030027 (2020).
[23]W. P. Bassett, B. P. Johnson, N. K. Neelakantan, S. Suslick, and D. D. Dlott, Appl. Phys. Lett. **111**, 061902 (2017).
[24]W. P. Bassett, B. P. Johnson, L. Salvati, and D. D. Dlott, J. Appl. Phys. **125**, 215904 (2019).
[25]H. K. Springer, S. Bastea, A. L. Nichols, C. M. Tarver, and J. E. Reaugh, Propellants, Explos., Pyrotech. **43**, 805 (2018).
[26]H. K. Springer, C. M. Tarver, and S. Bastea, AIP Conf. Proc. **1793**, 080002 (2017).
[27]N. K. Rai and H. S. Udaykumar, Phys. Fluids **31**, 016103 (2019).
[28]Y. Nguyen, P. Seshadri, O. Sen, D. B. Hardin, C. D. Molek, and H. Udaykumar, J. Appl. Phys. **131**, 055906 (2022).
[29]S. Roy, N. K. Rai, O. Sen, D. B. Hardin, A. S. Diggs, and H. S. Udaykumar, Shock Waves **30**, 349 (2020).
[30]C. Y. Li, B. W. Hamilton, and A. Strachan, J. Appl. Phys. **127**, 175902 (2020).
[31]G. A. Levesque and P. Vitello, Propellants, Explos., Pyrotech. **40**, 303 (2015).
[32]B. M. Patterson, L. Kuettner, K. Henderson, J. D. Yeager, and L. Hill, Propellants, Explos., Pyrotech. **47**, e202100340 (2022).
[33]P. C. H. Nguyen, Y. T. Nguyen, P. K. Seshadri, J. B. Choi, H. S. Udaykumar, and S. Baek, Propellants, Explos., Pyrotech. **48**, e202200268 (2023).
[34]Y. T. Nguyen, P. K. Seshadri, O. Sen, D. B. Hardin, C. D. Molek, and H. S. Udaykumar, J. Appl. Phys. **131**, 215903 (2022).
[35]P. Das, P. Zhao, D. Perera, T. Sewell, and H. S. Udaykumar, J. Appl. Phys. **130**, 085901 (2021).
[36]N. Rai, S. Koundinyan, O. Sen, I. Schweigert, B. Henson, and H. Udaykumar, Combust. Flame **219**, 225 (2020).
[37]C. D. Molek, E. J. Welle, D. B. Hardin, J. O. Mares, and J. P. Vitarelli, *Proceedings of the 16th Symposium (International) on Detonation ONR-43-5762-19* (Office of Naval Research, 2018), p. 60.
[38]H. R. James, Propellants, Explos., Pyrotech. **21**, 8 (1996).
[39]E. J. Welle, O. Sen, S. Roy, N. Rai, C. Molek, and H. S. Udaykumar, *44th International Pyrotechnics Seminar* (International Pyrotechnics Society, 2019).
[40]B. F. Henson, L. Smilowitz, J. J. Romero, and B. W. Asay, AIP Conf. Proc. **1195**, 257 (2009).
[41]C. M. Tarver and T. D. Tran, Combust. Flame **137**, 50 (2004).
[42]R. Menikoff, Combust. Theory Modell. **10**, 1003 (2006).
[43]O. Sen, N. K. Rai, A. S. Diggs, D. B. Hardin, and H. S. Udaykumar, J. Appl. Phys. **124**, 085110 (2018).
[44]N. K. Rai and H. S. Udaykumar, J. Appl. Phys. **118**, 245905 (2015).
[45]A. Kapahi, S. Sambasivan, and H. S. Udaykumar, J. Comput. Phys. **241**, 308 (2013).
[46]R. Menikoff and T. D. Sewell, Combust. Theory Modell. **6**, 103 (2002).
[47]T. D. Sewell and R. Menikoff, AIP Conf. Proc. **706**, 157 (2004).
[48]S. Sambasivan, A. Kapahi, and H. S. Udaykumar, J. Comput. Phys. **235**, 334 (2013).
[49]C. W. Shu, T. A. Zang, G. Erlebacher, D. Whitaker, and S. Osher, Appl. Numer. Math. **9**, 45 (1992).
[50]S. Gottlieb and C. W. Shu, Math. Comput. **67**, 73 (1998).
[51]S. Roy, N. K. Rai, O. Sen, and H. S. Udaykumar, Shock Waves **30**, 443 (2020).
[52]R. R. Wixom, A. S. Tappan, A. L. Brundage, R. Knepper, M. B. Ritchey, J. R. Michael, and M. J. Rye, J. Mater. Res. **25**, 1362 (2010).
[53]A. Nassar, N. K. Rai, O. Sen, and H. S. Udaykumar, Shock Waves **29**, 537 (2019).
[54]F. Walker and R. Wasley, Propellants, Explos., Pyrotech. **1**, 73 (1976).
[55]A. Kapahi and H. S. Udaykumar, Shock Waves **25**, 177 (2015).
[56]O. Sen, S. Davis, G. Jacobs, and H. S. Udaykumar, J. Comput. Phys. **294**, 585 (2015).
[57]E. L. Lee and C. M. Tarver, Phys. Fluids **23**, 2362 (1980).
[58]R. Menikoff, "JWL Equation of State," Report No. LA-UR-15-29536 (Los Alamos National Laboratory, 2015).
[59]E. J. Welle, C. D. Molek, R. R. Wixom, P. Samuels, and J. T. Langhals, *Proceedings of 15th International Detonation Symposium ONR-43-280-15* (Office of Naval Research, 2014), p. 71.
[60]N. J. Gaul, M. K. Cowles, H. Cho, K. Choi, and D. Lamb, *International Design Engineering Technical Conferences and Computers and Information in Engineering Conference* (American Society of Mechanical Engineers, 2015), p. V02BT03A060.
[61]O. Sen, N. J. Gaul, K. K. Choi, G. Jacobs, and H. S. Udaykumar, J. Comput. Phys. **336**, 235 (2017).
[62]G. James, D. Witten, T. Hastie, and R. Tibshirani, Springer Texts in Statistics (SPRINGER, 2013), Vol. 112. https://link.springer.com/book/10.1007/978-1-0716-1418-1